

# Halo heating from fluctuating gas in a model dwarf

Mahmoud Hashim,<sup>1</sup> Amr A. El-Zant,<sup>1\*</sup> Jonathan Freundlich,<sup>2</sup> Justin I. Read<sup>3</sup> and Françoise Combes<sup>4,5</sup>

<sup>1</sup>*Centre for Theoretical Physics, The British University in Egypt, Sherouk City, 11837 Cairo, Egypt*

<sup>2</sup>*Observatoire Astronomique, Université de Strasbourg, CNRS, 11 rue de l'Université, 67000 Strasbourg, France*

<sup>3</sup>*Department of Physics, University of Surrey, Guildford, GU2 7XH, United Kingdom*

<sup>4</sup>*LERMA, Observatoire de Paris, CNRS, PSL Univ., Sorbonne Univ., F-75014 Paris, France*

<sup>5</sup>*Collège de France, 11 place Marcelin Berthelot, F-75005 Paris, France*

Accepted XXX. Received YYY; in original form ZZZ

## ABSTRACT

The cold dark matter (CDM) structure formation scenario faces challenges on (sub)galactic scales, central among them being the ‘cusp-core’ problem. A known remedy, driving CDM out of galactic centres, invokes interactions with baryons, through fluctuations in the gravitational potential arising from feedback or orbiting clumps of gas or stars. Here we interpret core formation in a hydrodynamic simulation in terms of a theoretical formulation, which may be considered a generalisation of Chandrasekhar’s theory of two body relaxation to the case when the density fluctuations do not arise from white noise; it presents a simple characterisation of the effects of complex hydrodynamics and ‘subgrid physics’. The power spectrum of gaseous fluctuations is found to follow a power law over a range of scales, appropriate for a fully turbulent compressible medium. The potential fluctuations leading to core formation are nearly normally distributed, which allows for the energy transfer leading to core formation to be described as a standard diffusion process, initially increasing the velocity dispersion of test particles as in Chandrasekhar’s theory. We calculate the energy transfer from the fluctuating gas to the halo and find it consistent with theoretical expectations. We also examine how the initial kinetic energy input to halo particles is redistributed to form a core. The temporal mass decrease inside the forming core may be fit by an exponential form; a simple prescription based on our model associates the characteristic timescale with an energy relaxation time. We compare the resulting theoretical density distribution with that in the simulation.

**Key words:** dark matter – galaxies: haloes – galaxies: evolution

## 1 INTRODUCTION

In the standard cosmological scenario, CDM particles decouple while non-relativistic from the primordial thermal bath. Their consequently small speeds allow for a clustering that agrees well with an impressive array of observations on large scales (Frenk & White 2012). But this same ‘coldness’ leads to excessive central densities in the nonlinear regime. As soon as they could resolve the central regions, simulations showed that CDM haloes were endowed with central density cusps, with their density diverging towards the centre (Dubinski & Carlberg 1991; Warren et al. 1992). It subsequently transpired that this reflected nearly ‘universal’, self-similar, behaviour; with the density profiles of haloes at different masses, identified at various epochs, well fit with by simple empirical formulae (Navarro et al. 1996b). But the central density cusps seemed too dense to match those inferred for dark matter dominated galaxies, like low-surface-brightness and dwarf galaxies (Moore 1994; Flores & Primack 1994).

This ‘cusp-core’ problem is central to the low-redshift small-scale issues associated with CDM structure formation, which have attracted much attention during the past decades, as its resolution may simultaneously alleviate other puzzles associated with small scale structure in CDM simulations, such as the so-called ‘too-big-to-fail’

problem (Read et al. 2006; Boylan-Kolchin et al. 2011; Ogiya & Burkert 2015; for general reviews see, e.g., Del Popolo & Le Delliou 2017; Bullock & Boylan-Kolchin 2017; Salucci 2019). CDM-based simulations also predict a general over-abundance of small haloes compared to small galaxies. However, down to the resolution level of current cosmological simulations and expected minimal galaxy mass, this issue has been claimed to be less severe as small Milky Way satellite galaxies are being discovered and counted in (e.g., Nadler et al. 2020).

Assuming that the data has not been misinterpreted (e.g. Oman et al. 2019), solutions to the aforementioned problems can be principally divided into two sets; those modifying the underlying dark matter particle physics model and those invoking gravitationally mediated CDM interaction with baryons. The most popular of the first category have been warm dark matter and self interacting dark matter, and the more recently topical fuzzy dark matter. The simplest models of the latter type have problems explaining core scaling relations in galaxies (Deng et al. 2018; Burkert 2020; Bar et al. 2021), and warm dark matter does not generally succeed in producing central density cores at all, as cold collapse occurs unless the dark matter is ‘warm’ enough to prevent the halo at hand from forming in the first place (Macciò et al. 2012). Warm dark matter may make baryonic core formation easier, due to lower halo concentrations, but this is debated since warm dark matter also acts to suppress early star

\* E-mail: amr.elzant@bue.edu.eg

formation (Governato et al. 2015). In general particle physics based modifications to the standard structure formation scenario invoking warm dark matter or fuzzy dark matter, have been more successful in alleviating the apparent over-abundance of small scale structure in CDM-based structure formation. But this, instead of being a strong point, has now joined Lyman- $\alpha$  constraints (e.g., Iršič et al. 2017a,b) and strong lensing (e.g., Gilman et al. 2020) in setting limits on the efficacy of such models (Simon & Geha 2007; Kopolov et al. 2008; Kim et al. 2018; Read & Erkal 2019; Newton et al. 2021; Nadler et al. 2020, 2021). In addition, models where small haloes are invariably expected to come with significant cores, such as in the fuzzy dark matter scenario, may be constrained by the survival of Milky Way satellites with eccentric trajectories that take them to the host halo’s central region (Errani et al. 2023). Interacting dark matter-based models on the other hand generically suffer from eventual gravothermal contraction of cores, which are not easily avoided for all relevant spatial and time scales (Burkert 2000; Kochanek & White 2000; Turner et al. 2021), (although, fine tuning aside, this may actually be considered a phenomenological strong point of a subset of such models; Yang et al. 2022).

A non-negligible scattering cross-section between standard model particles and dark matter has also been proposed (Famaey et al. 2020; Salucci et al. 2020), although this option has not been as fully investigated so far,

On the other hand, gravitational coupling between dark matter and baryons has long been known to be effective in transforming CDM cusps into cores. Its main shortcoming however comes from the complex physics and the associated uncertainties in the parameters involved. Indeed, cusp-core transformation through such coupling come in three different forms: one time mass blowout due to a single burst of energy feedback (Navarro et al. 1996a, and more recently Freundlich et al. 2020a and Li et al. 2022); the pumping of energy from (gaseous or stellar) baryonic clumps to CDM via dynamical friction (El-Zant et al. 2001, 2004); and density and potential fluctuations in feedback-driven gas during galaxy formation (Read & Gilmore 2005; Pontzen & Governato 2014). Despite the apparent similarity of the first and third mechanisms (as they both invoke feedback), it is the last two that are in fact more closely related at a deeper level — as they both involve a long-lived fluctuations progressively heating the CDM on timescales much longer than that of a single feedback starburst, as discussed in El-Zant et al. (2016).

Dynamical friction heating is nevertheless expected to be observationally distinct from supernova heating since the latter correlates with star formation (e.g. Read et al. 2019) while the former does not, and both may act in tandem during galaxy formation (Orkney et al. 2021; Dekel et al. 2021; Ogiya & Nagai 2022). In the particular case of dwarf galaxies, there is mounting observational evidence for dark matter heating from impulsive, ‘bursty’, star formation, ubiquitous in dwarfs below a stellar mass of  $M_* \sim 10^8 M_\odot$  (e.g. Collins & Read 2022). Indeed, there is an observed anticorrelation between the inner dark matter density of dwarfs and their stellar-to-halo mass ratio  $M_*/M_{200}$  (Read et al. 2019; Bouché et al. 2022), which is a proxy for the amount of star formation – and therefore dark matter heating – that has taken place (e.g. Peñarrubia et al. 2012; Di Cintio et al. 2014; Freundlich et al. 2020b). This may favour a scenario of feedback-driven core formation in such galaxies.

As conjectured in El-Zant et al. (2016), it may be possible to understand the process of feedback-driven core formation with repeated bursts from first principles, bypassing the uncertain complexities of ‘gastrophysics’ and its various subgrid implementations. Indeed the stochastic dynamical model presented there suggested that the process of core formation depended primarily on just two parameters,

namely the gas mass fraction and the strength of the fluctuations characterised by the normalisation of a power-law power spectrum. It is our purpose here to study the properties of feedback-driven fluctuations in a full hydrodynamic simulation where a cusp-core transformation occurs, with the aforementioned model forming an interpretive framework and guide. Thus testing, in the process, its assumptions and predictions.

## 2 MODELLING HALO HEATING FROM GAS FLUCTUATIONS

### 2.1 Physical setting

The general picture envisioned, in El-Zant et al. (2016), and here, is that of a gas settling into a CDM halo. As it contracts, a critical density is reached, leading to star formation and consequent starburst. The star formation process assumed is akin to that described in Teysier et al. (2013) and Read et al. (2016). Namely, the threshold is considered high enough so that most star formation does not occur in a few bursts, but instead repetitively over a long timespan. This leads to sustained density and mass fluctuations in the gas that appear amenable to a description in terms of a stationary stochastic process over the timescale of the simulation.

If, to a first approximation, the gas density is assumed to be isotropic and homogeneous when averaged over large spatial or time scales, with average density  $\rho_0$ , then the mass fluctuations within a spatial scale  $R$  can (as in characterising cosmic structure) be characterized by a dispersion

$$\sigma_R^2 = \frac{1}{2\pi^2} \int_0^\infty W^2(k, R) \mathcal{P}(k) k^2 dk, \quad (1)$$

where  $\mathcal{P}(k)$  is the equal time power spectrum of the density fluctuations  $\delta\rho(\mathbf{r}, t)/\rho_0 - 1$ , and  $W$  is a Fourier filter function. If the fluctuations furthermore constitute a stationary Gaussian random process, this is all what one needs to know to completely characterise them. The stochastic dynamics can likewise be described completely in terms of the first and second moment statistics of the force field, which are easily obtainable from the Poisson equations: in particular, the  $k$ -modes of the potential fluctuations are related to those of the density by  $\phi_{\mathbf{k}} = -4\pi G \rho_0 \delta_{\mathbf{k}} k^{-2}$ , as discussed in El-Zant et al. (2016) and, in another context, in El-Zant et al. (2020). As shown in the latter work, this formulation can also describe standard two-body relaxation. As such, it can be used to calculate the effect of fluctuations arising from the presence of a collection of massive particles on a system of lighter ones. Relaxation in this context ‘heats’ the light particles, by increasing their velocity dispersion, while the heavier particles lose energy via dynamical friction. The general theoretical framework used here thus also applies to dynamical friction heating of the halo in the presence of massive clumps. The relevant power spectrum of density fluctuations, in that case, is flat (white noise) over scales larger than the maximum size of the (monolithic) clumps. Thus the description in terms of dynamical friction heating is more relevant when the gas fluctuations can be described in terms of a system of long lived distinct clumps with sizes significantly smaller than the region where the core forms.

When feedback is strong, and the gas fully turbulent on scales relevant to core formation, the spectrum of density fluctuations may be assumed to be approximated by a power law over such scales. As in the white noise case, the fluctuations lead to energy transfer from the gas to the halo particles, which drives the transformation of the latter’s problematic central cusp into a core. The energy transfer may still be described in particularly simple terms, reminiscent of

Chandrasekhar’s theory of two body relaxation; for a given halo and power spectrum  $\mathcal{P} \propto k^{-n}$ , the associated relaxation time  $t_{\text{relax}}$  is predicted to principally depend just on the normalization of that spectrum at the minimal wavenumber  $\mathcal{P}(k_m)$  (at which the power law breaks), and the average gas density  $\rho_0$ . More concretely, for a halo particle moving with an unperturbed speed  $v_p$  in a field of gas fluctuations carried by bulk flows moving with characteristic speed  $v_r$  relative to it, one finds

$$t_{\text{relax}} = \frac{nv_r v_p^2}{8\pi(G\rho_0)^2\mathcal{P}(k_m)}. \quad (2)$$

This is the timescale for the random velocity gained by a CDM particle, as a result of its motion in the stochastic force field born of gas fluctuations, to reach the unperturbed characteristic speed  $v_p$ . It is analogous to the standard relaxation time. In fact equation (2) reduces to Chandrasekhar’s formula for a white noise spectrum ( $n = 0$ ), with Coulomb logarithm determined by the ratio of maximal to minimal wavenumber cutoffs (El-Zant et al. 2020, Section 2). Also, as equation (2) is derived using Fourier transformation, which is transitionally invariant and therefore necessarily leads to loss of spatial information, it is (like Chandrasekhar’s formula) strictly valid only for an infinite homogeneous system with a constant level of fluctuations. In applying it to a real system, we will thus assume an approach that is akin to that widely invoked with the use of Chandrasekhar’s theory in an inhomogeneous system, where it is customary to assume that the variation of the relaxation time with position is accounted for by the density variation. In our formulation of Chandrasekhar’s theory, referred to above, this would mean keeping  $n = 0$  and the ratio of maximal to minimal wavenumber fixed, while adjusting the density to account for radial variations in the relaxation time. Analogously, we will keep the power spectrum parameters in equation (2) fixed and assume that the spatial variation of the energy input to the dark matter from the gas fluctuations can be accounted for by variation in the density.

To account for the radial change in the average gas density in a realistic system, we define the average density, at a given time, within a sphere with radial coordinate  $r$  by

$$\rho_0(r, t) = \langle \rho_g(\mathbf{r}, t) \rangle_{|\mathbf{r}| < r}, \quad (3)$$

where  $\rho_g(\mathbf{r}, t)$  is the local gas density and the average is evaluated within the volume enclosed by  $r = |\mathbf{r}|$ . A further average over time results in  $\rho_0(r)$ . If the averaging is not evaluated over a sphere centered at the origin, but over spheres with centres at radial coordinate  $r$  and radius  $r_{\text{av}}$ , an analogous average may also be defined (as in equation 9). In Section 4.2, we examine three different approximations for an effective  $\rho_0$ , in order to account for changes of relaxation time with radius while using equation (2): one associated with what we will call global energy transfer, i.e. with  $\rho_0$  a constant corresponding to an average inside an energy transfer saturation radius  $r_{\text{sat}} \gtrsim r_s$ , which turns out to be plausible, given the slow variation of average gas density inside  $\sim r_s$  and subsequent sharp drop (Fig. 3); a local approximation, which does not work; and one involving averages over radius  $r_{\text{av}} = r_s \approx 1\text{kpc} \approx 1/k_m$ , which we will find works best (Fig. 8). This is perhaps not surprising given the aforementioned gas density variation, and given that equation (2) implies that modes near  $k_m$  contribute most to the relaxation process. (It in fact arises from a low- $k$  ‘effective theory’, as discussed further in the penultimate paragraph of Appendix A).

The characteristic velocity  $v_r$  appearing in equation (2) is estimated through the ‘sweeping’ approximation, long used in turbulence theory (Taylor 1938; Kraichnan 1964; Tennekes 1975) and invoked by El-Zant et al. (2016). It assumes that the equal-time spa-

tial statistics of the fluctuation field are swept (‘frozen in’) into the time domain through large scale fluid flows. In this picture  $v_r$  consists of random and regular velocity components  $U$  and  $V$ , such that  $v_r = \sqrt{U^2 + V^2}$  that are characteristic of those flow. In our case, since the halo particles are also moving with respect to the gaseous flows, the characteristic  $v_r$  may be considered to include such motions.<sup>1</sup> We test this assumption in Section 3.3.

In the context of the formulation outlined in this section, the timescale of significant central halo transformation, from cusp to core, should scale as in equation 2, with parameters as defined above. Controlled simulations (using the Hernquist-Ostriker code (Hernquist & Ostriker 1992), whereby Gaussian random noise was applied to particles of live CDM haloes, produced cores on the expected timescale, when the haloes were kept strictly spherical (El-Zant et al. 2016).<sup>2</sup>

## 2.2 Numerical implementation

We wish to examine feedback-driven gas fluctuations in a full hydrodynamic simulation, to find out whether their characteristics and their effects may fit the picture outlined above. To facilitate the isolation of the principal features, we focus on the case of an isolated galaxy. Its parameters (Table 1) are chosen to correspond to those of dwarf galaxies, where dark matter dominates even in the central regions and the discrepancy between the inferred density and a centrally concentrated halo profile seems particularly clear.

The simulation of the isolated dwarf is set up and run with the RAMSES adaptive mesh refinement code (Teyssier 2002), and already presented in Read et al. (2016). We use ‘Run M9c224e6’ from that paper, which has 281 time outputs regularly spaced over a timespan of 13.7 Gyr. The initial condition for this simulation assumes a NFW dark matter halo (Navarro et al. 1996b) with total mass inside the virial radius  $M_{200} = 10^9 M_\odot$  and concentration parameter  $c_{200} = 22.23$ . A fraction  $f_b = 0.15$  of that mass ( $M_g(r_{\text{vir}}) = 0.15 \times 10^9 M_\odot$ ), is in gas that is initially in hydrostatic equilibrium, with a metallicity of  $10^{-3} Z_\odot$  and some angular momentum set to match median expectations in a  $\Lambda$ CDM cosmology. While the simulation assumes that the dwarf galaxy contains the Universal baryon fraction out to its virial radius, the ratio between the gas mass initially within the region of interest for core formation ( $\sim 1$  kpc) and the mass within the virial radius is much lower, and thus consistent with observational constraints (e.g. Read & Trentham 2005). At the start of the simulation, the gas rapidly cools and collapses, then re-expands under the influence of feedback. In the process, the central gas mass fraction further decreases (cf. Section 3.1).

The sub-grid model for star formation and feedback is described in detail in Read et al. (2016). Briefly, star formation follows a Schmidt relation with a star formation efficiency per free fall time of  $\epsilon_{\text{ff}} = 0.1$  and a density threshold for star formation of  $\rho_* = 300 \text{ atoms cm}^{-3}$ . The stellar feedback model is as in Agertz et al. (2013) and includes a model for Type II and Type Ia supernovae, stellar winds and radiation pressure. The simulation resolution was chosen to capture

<sup>1</sup> In principle, each fluctuating mode may have its own sweeping speed and the velocity distribution of the particles can be taken into account, as in El-Zant et al. (2020). We do not consider this more complex case here.

<sup>2</sup> When this condition was relaxed, the timescales for core formation were found to be about an order of magnitude shorter. But the scaling with the normalisation of the power spectrum and average density, as reflected in equation (2), remained. As noted in Section 4.3, we find no evidence of such accelerated (relative to the relaxation time) core formation rate here.

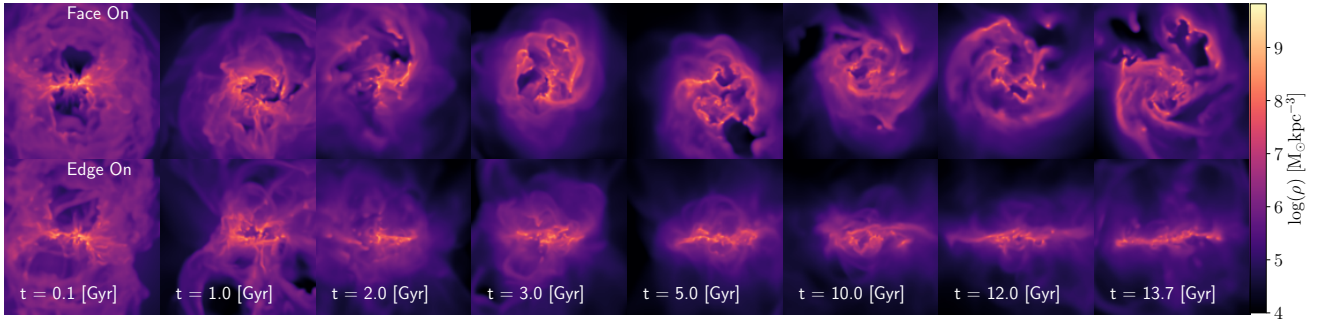


**Figure 1.** Gas projected density map inside a box of length 5 kpc (2.5 kpc on a side from the centre of the halo). The gas contracts from the initial NFW profile, then much of it is expelled from the inner region during the first few hundred Myr. It gradually settles into a disk-like configuration, but its distribution fluctuates over time.

**Table 1.** Initial profile parameters.

NFW scale length	$r_s$	0.88 kpc
NFW characteristic density	$\rho_s$	$5.34 \times 10^7 \text{ M}_\odot \text{ kpc}^{-3}$
Concentration parameter	$c$	22.23
Mass within the virial radius	$M_{\text{vir}}$	$10^9 \text{ M}_\odot$
Baryonic mass fraction	$f_b$	0.15

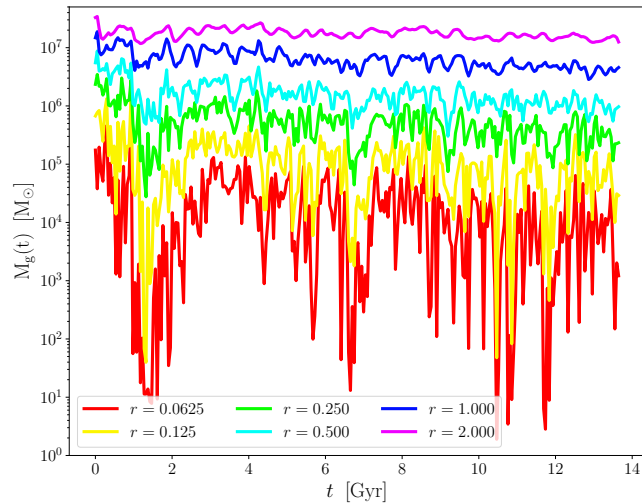


**Figure 2.** Time variation of the gas mass enclosed within different radii  $r$  (in kpc), suggesting a quasi-stationary stochastic process.

momentum driving from individual supernovae events, with a gas spatial resolution (at highest mesh refinement) of  $\Delta x \sim 4 \text{ pc}$  and a mass resolution in gas, stars and dark matter of  $m_g = 60 \text{ M}_\odot$  and  $m_* = M_{\text{DM}} = 250 \text{ M}_\odot$ , respectively. This allows individual star formation events to be resolved, injecting stellar feedback to the interstellar medium in the correct locations at the correct times.

### 3 CHARACTERIZING THE GAS FLUCTUATIONS

In order to apply the physical model described above, leading to equation (2), we need to know the average gas density  $\rho_0$ . We also

need to evaluate the power spectrum of the gas fluctuations and find out whether it may indeed be adequately described by a power-law, in which case we need to estimate values for its normalization  $\mathcal{P}(k_m)$  and index  $n$ , and verify that the spatial spectrum is relevant in describing the temporal fluctuations. This is the objective of this section.

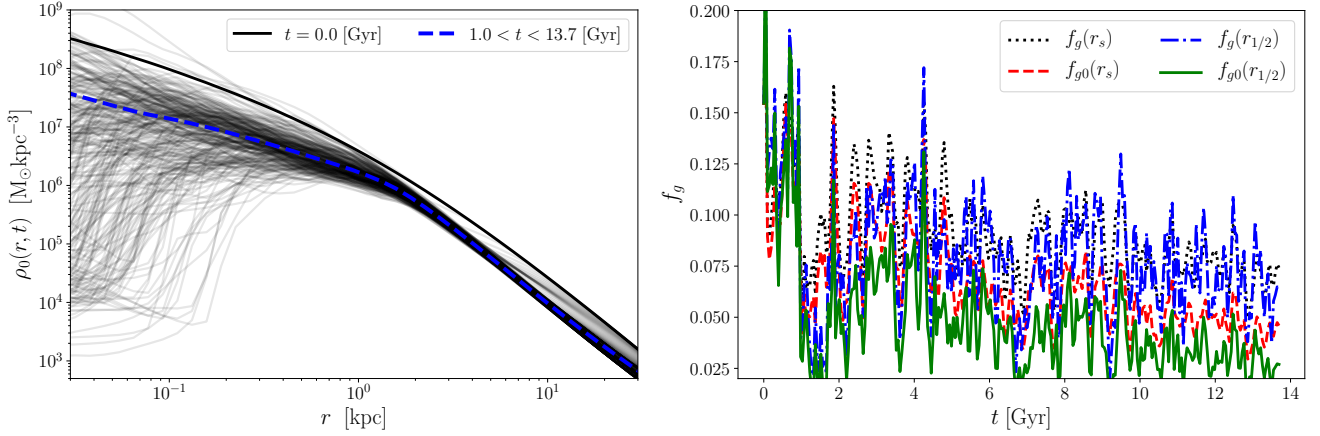
#### 3.1 Gas density and mass over time

Fig. 1 shows gas density contrast maps, within a 5 kpc box, 2.5 kpc on a side from the halo centre<sup>3</sup>. The gas initially contracts from an NFW profile with scale length  $r_s$  until the critical threshold for star formation is reached. The fluid is then driven by the nascent feedback, much of it driven completely out of the region delineated by  $r_s$ ; the gas mass inside  $\sim r_s$  decreases to less than half its initial value (but the dark matter mass is largely unaffected, decreasing only by about 20% within  $r_s$ , and thus the ratio decreases significantly, as shown in the right hand panel of Fig. 3). After that, the gas mass inside  $\sim r_s$  is relatively well conserved. Variations in the gas mass enclosed within a given radius then principally arise from a pattern of fluctuations (gaseous blobs) materialising on a large range of scales. The gas progressively settles into a disk-like configuration, but the mass fluctuations remain sustained and steady.

The assumption that the fluctuations form a quasi-steady stochastic process is suggested by Fig. 2, showing the mass variation within different radii over time. The mass fluctuations persist in time but diminish with radius, as higher mass scales are reached. Significant variations on larger time-scales persist however. They correspond to large scale flows. In the context of the model of El-Zant et al. (2016) (recapped in Section 2.1), such large scale motions ‘sweep’ the smaller scale fluctuations with the characteristic speed  $v_r$  (equation 2). For the description of the effect of the gas fluctuations on the halo particles in terms of a standard diffusion process (leading to relaxation timescales in the form of equation 2) to be complete, the statistics of the stationary stochastic process should also be entirely described by averages and dispersions, as in a Gaussian random process. This is examined in Appendix A.

The gas density inside spheres of radius  $r$  is shown in Fig. 3, as a functions of time. After the initial outflow during the first few hundred Myr, the averaged (over time) gas profile is only mildly varying with

<sup>3</sup> Unless otherwise stated, all centering here refers to the halo centre located using the shrinking sphere method.



**Figure 3.** *Left:* Average gas density inside radius  $r$ ,  $\rho_0(r, t)$ , for all snapshots, obtained by using equation (3). The dashed line is a time average over the indicated interval, which corresponds to the simulation time beyond an initial non-equilibrium phase through which much of the gas is blown out of the region inside  $r_s \simeq 1$  kpc. The time averaged profile is only mildly varying inside  $r_s$ . *Right:* Ratio of the gas to combined gas and dark matter masses  $f_g = M_g / (M_g + M_d)$ , with  $f_g(r_s)$  denoting the fraction inside  $r_s$ ; thus here  $M_g = M_g(< r_s, t)$  and  $M_d = M_d(< r_s, t)$ , while  $f_{g0}$  denotes the ratio of the gas mass to the initial total mass enclosed:  $f_{g0}(r_s) = M_g(< r_s, t) / [M_g(r_s, 0) + M_d(< r_s, 0)]$ . Similarly  $f_g(r_{1/2})$  and  $f_{g0}(r_{1/2})$  refer to those ratios inside the half mass radius of the stellar component that forms from the repeated starbursts,  $r_{1/2} \simeq 0.5$  kpc, and which physically correlates with the scale of the relatively steady gas density associated with strong fluctuations.

radius inside the initial NFW scale length ( $r_s = 0.88$  kpc), and then starts decreasing rapidly beyond that. Any core that forms is expected to be of the order of the scale length of the cusp, which renders the assumptions in El-Zant et al. (2016) (discussed in Section 2.1.2 therein), plausible. One may for instance attempt to estimate the relaxation time using equation (2) with mean density  $\rho_0$  evaluated at radius  $\gtrsim r_s$ , as the sharp decrease in density beyond that scale suggests that fluctuations in the gas at larger radii would contribute little to the overall variations in the gas potential and associated energy input to the central halo.

In Section 4, we estimate that this may indeed be a good approximation. Here we note that there are two theoretically independent reasons why, given the parameters of the simulation, a core is expected to form on a scale of order 1 kpc. For, even if the gas density does not drop beyond  $r \gtrsim r_s$ , and strong fluctuations are present much beyond that radius, the resulting stochastic perturbations are expected to have a major dynamical effect only up to scale of order  $r_s$ . This was in fact found to be the case even when the amplitude of the fluctuations (as fixed by the normalization of the power spectrum) were increased well beyond the minimum level required to significantly affect the inner halo profile (cf. Fig. 6 of El-Zant et al. (2016)). The phenomenon is likely due to the transition to an isothermal profile in an NFW halo at  $r \simeq r_s$ , which is relatively stable against fluctuations, as the differential energy distribution tends to an exponential form (cf. Appendix C4). This phenomenon relates to the effect of the fluctuations. The other reason why a core that forms out of a cusp here should have radial scale of order 1 kpc has to do with the existence of fluctuations in a realistic system: the extent of the spatial scale where the gas density and density contrasts are large is characteristic of the half mass radius  $r_{1/2}$  of the stellar component that forms from the repeated starbursts. In our case about 0.5 kpc. Because of this, we will be able to define (in relation to Fig. 7) an energy input saturation radius, of order  $\simeq 2r_{1/2}$ , which results from the decreasing gas density and level of fluctuations. Beyond it, there is negligible energy transfer from gas to halo.

The right panel of Fig. 3 shows the fraction of gas inside both  $r_s$  and  $r_{1/2}$ . We note that due to the small variation of the gas density averaged over radius, the lines closely correspond to one another.

In addition, after the gas loss associated with the initial blowout phase, the gas fraction decreases to about half its initial value. Thus, any effect due to core formation will result from fluctuations from a rather small gas fraction in the inner regions. The efficacy of this perhaps surprisingly small central gas fraction in modifying the dark matter dynamics is in fact a generic prediction of our theoretical framework, provided the strength of the gas fluctuations is at the level of the fiducial model in El-Zant et al. (2016) (cf. Section 2.1.2 and 4.4.2 there). Below, we will find that the fluctuation levels in the present simulation, as measured by the normalisation of the power spectrum, are in indeed consistent with those assumed in that fiducial model.

### 3.2 Power spectra

We now proceed to determine the power spectrum of the density fluctuations qualitatively probed above. We evaluate it in the following way. For a given time snapshot, we consider gas cells within a cubical box of extent 2.5 kpc on each side from the origin.<sup>4</sup> We assign each cell, depending on its radial location, to a spherical shell. The average gas density inside the shell  $\rho_{sh}$  is then subtracted from that at a given cell  $\rho_{cl}$ . The density contrast in each cell  $\delta_{cl} = \rho_{cl} / \rho_{sh} - 1$  is evaluated, and the Fourier transform is taken over the cells and squared in the usual manner, to obtain the power spectrum (using the Fourier convention employed in El-Zant et al. 2016). This is done for each time snapshot, and the results are averaged over a chosen set of snapshots. The outcome is shown in Fig. 4. The spectrum follows a power-law form over a range of scales, with an index consistent with that assumed in the fiducial model of El-Zant et al. (2016), where it was assumed to correspond to 2.4. If we take  $k_m \simeq 2 \text{ kpc}^{-1}$ , then  $\mathcal{P}(k_m) \simeq 4 \text{ kpc}^3$  (again close to what was assumed in the fiducial model of El-Zant et al. 2016, namely  $\mathcal{P}(k_m) = 4.6 \text{ kpc}^3$ ).

<sup>4</sup> Taken here to be the centre of the halo located through the shrinking sphere method. We have verified that the results are robust to displacements of that centre  $\lesssim 1$  kpc, and similar results are obtained when the gas centre of mass or shrinking sphere centres are used.

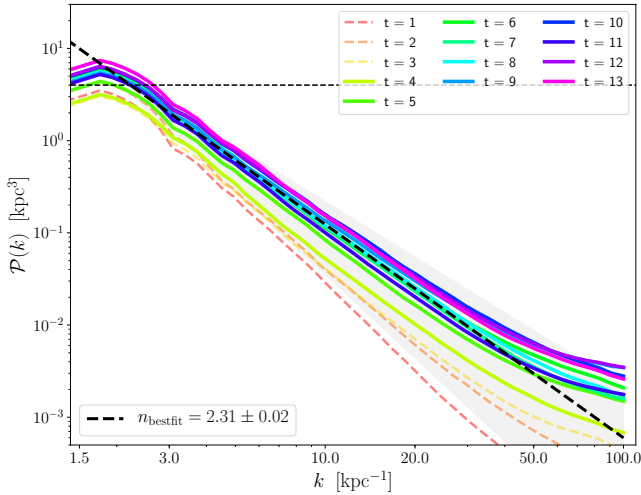


**Figure 4.** Power spectrum of gas density fluctuations, averaged over 1 Gyr intervals. The shaded region corresponds to variation of a power law  $\sim k^{-n}$ , with  $2 \leq n \leq 3$ ; the horizontal line corresponds to  $\mathcal{P}(k_m) = 4 \text{ kpc}^3$ . The spectrum follows a power-law form over a range of scales, with a best-fit exponential index  $n_{\text{bestfit}} = 2.31 \pm 0.02$  (black dashed line).

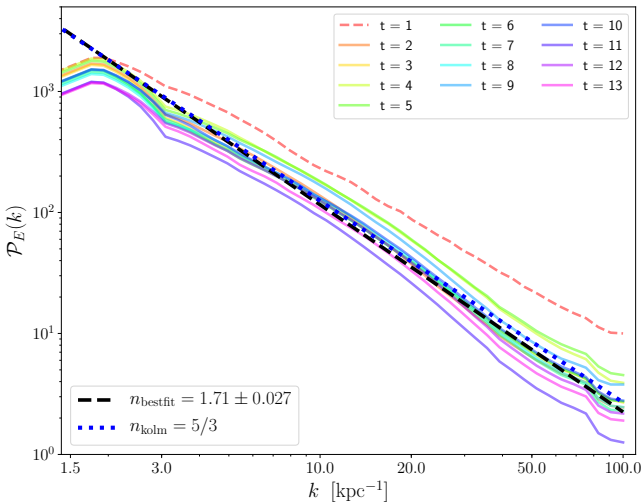


**Figure 5.** Kinetic energy power spectrum of gas motion with least squares best fit (black dashed line) and Kolmogorov spectrum ( $\propto k^{-5/3}$ ), blue dashed line). The spectrum is calculated through the square of the Fourier transform of  $\rho_{gi}^{1/2} \mathbf{v}_i$ , taken over gas cells  $i$  inside a 5 kpc box around the halo (shrinking sphere) centre. The agreement with the Kolmogorov form supports feedback-driven fluctuations having characteristics of fully developed turbulence.

The picture of fully turbulent feedback-driven fluctuations is supported by the near Kolmogorov form of the specific kinetic energy spectrum, shown in Fig. 5, which is followed for a large range in wave numbers. This spectrum persists even as the gaseous system evolves from a fully three dimensional configuration to disk-like form. Indeed [Grisdale et al. \(2017\)](#) found that it is present even in relatively quiescent phases, as long as feedback is also present (noting that the spectrum flattened when feedback is eliminated). In principle, turbulence may also be driven by self gravitating instabilities rather than feedback (e.g., [Yu et al. 2021](#); [Nusser & Silk 2022](#)). A simple

calculation of the gas Toomre parameter in the present case nevertheless suggests an absence of strong gravitational instabilities (see however [Inoue et al. 2016](#)).

In the context of our theoretical framework, a further (likely related) physical distinction may also be reflected in the shape of the density fluctuation power spectrum; for, as mentioned in Section 2.1, a flat (white noise) power spectrum corresponds to the limit when heating through dynamical friction coupling between monolithic clumps and the dark matter is the dominant process. In this case the clumps are long lived and distinct, and their maximum size is significantly smaller than the scale associated with the region where the cusp-core transformation takes place (and on which the spectrum takes the flat form). The steep power-law dependence that continues up to large scales, as found here, signals a preeminence of feedback driven fluctuations. Only at the largest scales ( $< k_m$ ) is a flattening of the spectrum recovered. (The flattening at large  $k$  denotes the start of the transition from the turbulent inertial range to the dissipation range, set here by the numerical resolution, given the small kinetic viscosity, and may reflect a 'bottleneck phenomenon', resulting from a pile-up of inefficiently dissipated energy as the transition is approached; [Falkovich 1994](#); [Schmidt et al. 2004](#); [Kritsuk et al. 2007](#).)

Finally, we note that the break in the kinetic energy power spectrum at  $k_m \approx 2 \text{ kpc}^{-1}$  is consistent with that inferred from Fig. 4, suggesting a demarcation between the turbulent scaling regime and the large scale flows that may carry the fluctuations into the time domain. We examine this issue of the transposition of the fluctuation characteristics from the spatial to temporal domains further in the next subsection.

### 3.3 RMS mass fluctuations

Our formulation of the dynamical effect of the gas fluctuations makes use of the sweeping and random sweeping approximations of turbulence theory, mentioned at the end of Section 2.1. At some level, this is analogous to an ergodic assumption, in the sense that statistical properties of the random field in the spatial domain are transferred into the time domain. If such an approximation is valid in our case, then we should expect the following: if the variance  $\sigma_R^2$  on the left hand side of equation (1) is calculated in the time domain over the simulation snapshots, it should correspond to the result obtained by plugging the equal-time power spectrum  $\mathcal{P}(k)$ , with parameters consistent with what is inferred above (Fig. 4), into the right hand side of equation (1).

In a stochastic process that is homogeneous in space and time, with the sweeping assumptions holding, the  $\sigma_R$  measured in the time domain (over sufficiently long time) will be invariant with respect to the centre it is measured from. This cannot be strictly the case here, however, since the average gas density is not strictly homogeneous, although the power spectrum of relative density fluctuations was found to be rather robust against changes in the centre of the box inside which it is calculated (Footnote 4). Furthermore, when attempting to match temporal fluctuations to those captured by spatial power spectra at given snapshots one needs to eliminate effects not captured by the frozen-in spectra. For example, the effect of fluctuations carried by rotational flows will be reduced when calculating  $\sigma_R$  in spheres anchored close to the centre of rotation, with little mass transiting through the shells (and those carried by large scale radial flows are enhanced). To account for such effects, we randomise the centre of the sphere within which the mass is calculated. The centres are, in practice, sampled from a homogeneous distribution within the radius of interest for core formation (1 kpc from the origin). We

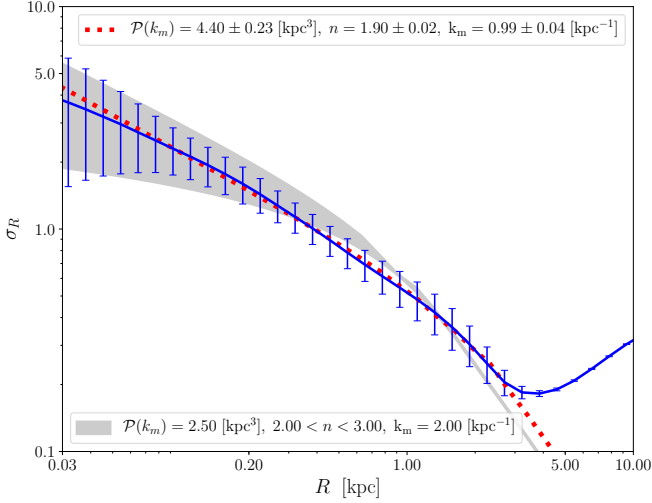


**Figure 6.** Gas mass dispersion at scale  $R$ ,  $\sigma_R^2 = \sum_i (M_i(R) - \langle M(R) \rangle_i)^2 / \langle M(R) \rangle_i^2$ , where  $i$  denotes different time snapshots, and  $M(R)$  is the mass inside a sphere of radius  $R$ . The centre of the sphere is randomized; chosen from a homogeneous distribution inside radius 1 kpc ( $\approx r_s$ ). The process is repeated for 80 realizations and the average  $\sigma_R$  over the realizations (solid line) and dispersion (error bars) are evaluated. The dotted line refers to a (least squares) best-fit using equation (1) with a power-law power spectrum and a top-hat filter, while the shaded region shows the variation with  $n$  in the range of the corresponding shaded region on Fig. 4, with moderately smaller normalization at  $k_m = 2 \text{ kpc}^{-1}$ . All fits assume  $\mathcal{P}(< k_m) = \mathcal{P}(k_m)$ . The power spectrum parameters, inferred here from simulation data in the time domain, are generally consistent with those of the equal-time power spectra of Fig. 4.

then conduct eighty different realizations of such randomisations and evaluate the average of the dispersion over the realisations.

Fig. 6 shows the result. The best-fit using equation (1) involves a power-law power spectrum with index  $n$  consistent with the lower limit in the shaded region of Fig. 4; and also with similar normalization  $\mathcal{P}(k_m)$ , but at smaller  $k_m$ . The change in  $k_m$ , by itself, is not expected to affect the dynamical effect of the fluctuations in the diffusion limit at the basis of our model (with consequence that the relaxation time in equation 2 does not directly depend on  $k_m$ ; see also Fig. 8 of El-Zant et al. 2016). On the other hand, the shaded area of Fig. 6 suggests that the mass dispersion is also consistent with larger values of  $k_m$ , but with mildly smaller normalization (which does moderately affect the relaxation time).

The general consistency of the parameters inferred here, in comparison with those obtained from the spatial power spectrum (Fig. 4), supports the contention that the spatial fluctuations are transported to the time domain in accordance with the sweeping assumptions (although the separation between the large scale ‘carrier flows’ and the transported fluctuations may not be sharp, and this may contribute to the smaller best fit  $k_m$  here). As we will see below, these parameters are also consistent with the actual energy input, from the fluctuating gas to the halo component, in the simulation studied here; in the sense that the inferred energy input is consistent with theoretical estimates using such values.

## 4 STOCHASTIC ENERGY TRANSFER AND CORE FORMATION

### 4.1 The relaxation time and its parameters

Now that we have estimates of the parameters entering equation (2), we can apply it in order to check whether it predicts significant effect for the model galaxy at hand. As a first estimate we simply assume  $v_p \approx v_r \approx v_c$ , where  $v_c = v_c(r_s)$  is the circular speed at  $r_s$  (close to the maximal rotation speed). If we furthermore use a value for  $\rho_0$  characteristic of the region when the density starts to decrease rapidly ( $r \gtrsim r_s$  from Fig. 3), we find

$$t_{\text{relax}} = 13.2 \text{ Gyr} \frac{n}{2.5} \left( \frac{v}{20 \text{ km/s}} \right)^3 \left( \frac{\mathcal{P}(k_m)}{3 \text{ kpc}^3} \right)^{-1} \left( \frac{\rho_0}{10^6 M_\odot/\text{kpc}^3} \right)^{-2}. \quad (4)$$

This suggests that gas fluctuations may have a significant effect on dark matter orbits within  $r_s$  on a timescale of the order of a Hubble time. If  $v_p$  and  $v_r$  are associated with the characteristic velocity dispersion (rather than  $v_c$ ), which is slightly larger (by a factor of about 10% at  $\sim r_s$ ), the above timescale increases by a factor of about  $(1.1)^{3/2}$ .

The timescale also increases if the characteristic speed of the halo particles relative to the gas  $v_r$  (cf. Section 2.1) is associated with gas velocities at  $\sim r_s$ , which are around 30 km/s (cf. Fig. A4). Because flows may take the gas well beyond  $r_s$ , gas velocities are generally larger than  $v_p$ . Once a rotating disk starts to materialise (Fig. 1), the regular component would also include gas rotation, in addition to the orbital speeds of the halo particles. Below, we will generally set  $v_r \approx 30 \text{ km/s}$ , but note that  $v_r$  should increase with radius inside  $r_s$ , and that it may generally be larger than the value adopted here when all the aforementioned motions and flows are taken into account.

The variation of the relaxation time with radius also depends on whether the energy input from gas fluctuations is assumed to be primarily global or local: the relaxation mechanism may in principle be global, in the sense of depending only on some effective  $\rho_0$ , corresponding to a space and time average over an appropriately chosen region (e.g., the region within which the feedback driven fluctuations are significant), or it may be local; depending on the local gas density  $\langle \rho_g \rangle(r)$  (averaged only over time). This is an issue we discuss further below, in connection to Fig. 8.

For a global energy input, the relaxation time depends only on variation in  $v_p$ , if  $v_r$  is kept fixed. with radius. If  $v_p$  is associated with  $v_c(r)$ , then within the initial NFW cusp  $v_p^2 \sim r/r_s$  increases by a factor of 6.25 as  $r/r_s$  goes from 0.1 to 1. If  $v_p$  is taken to correspond to the velocity dispersion then  $v_p^2 \sim -r/r_s \ln r/r_s$  deep inside the cusp, and increases by a factor of about 2.25 between  $r/r_s = 0.1$  and 1.

Thus, particles nearer to the centre are expected to be affected first by the fluctuations; if only simply because their initial velocities, and therefore the relaxation times required to affect them significantly, tend to be smaller. Core formation would thus proceed inside out, with mass distribution at larger radii affected at later times.

In what follows we evaluate the energy input in the simulation at hand and compare it with the theoretical picture sketched here; testing the ‘inside out’ scheme of core formation and the assumption of dependence of the energy transfer principally on the average density inside  $\sim r_s$  rather than the local density.

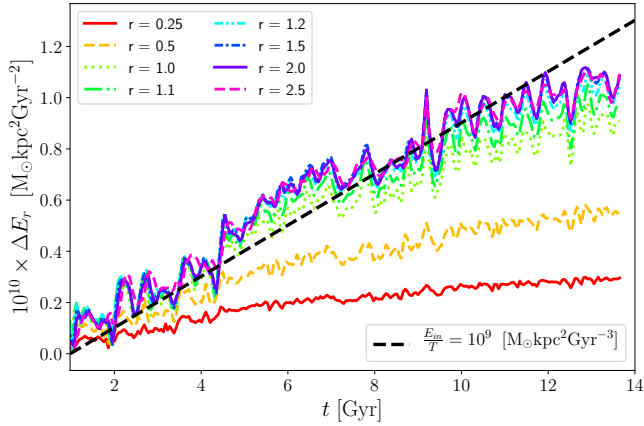


**Figure 7.** Energy input to halo particles from gas fluctuations inside indicated radii  $r$ .  $E_r$  is evaluated via equation (8), and measured from the temporal zero point  $t = t_{\text{diff}}$ , beyond which the diffusion limit may be assumed to hold. In line with the discussion following equation (5), we take  $t_{\text{diff}} = 1$  Gyr. In order to reduce fluctuations related to the precise choice of zero point, we calculate in practice  $\Delta E_r = E_r(t > t_{\text{diff}}) - \langle E_r \rangle_{t_{\text{diff}}}$ , where the average is taken in the interval  $0.5 \text{ Gyr} \leq t \leq 1.5 \text{ Gyr}$ . The dashed line indicates energy transfer through a stationary stochastic process, with parameter values appearing in equation (7). It assumes that energy input saturates around  $r_{\text{sat}} = 1.5 r_s \approx 1.3 \text{ kpc}$  (corresponding to the converging lines). For smaller radii, the lines flatten after a few Gyr due to mass and energy transfer resulting from particle migration towards larger radii.

## 4.2 Energy input

Equation (2) implies that a particle increases its velocity variance with time  $T$  as

$$\langle (\Delta v)^2 \rangle = \frac{8\pi(G\rho_0)^2 \mathcal{P}(k_m) T}{nv_r}. \quad (5)$$

The linear time dependence here is characteristic of a diffusion process. It is valid in the diffusion limit, which means that  $T \gg t_{\text{diff}} \equiv (v_r k_m)^{-1}$  (El-Zant et al. 2016). To account for this in practice, we will generally measure  $T$  and  $\langle (\Delta v)^2 \rangle$  from zero points at times  $t \geq t_{\text{diff}}$ . This is necessitated not just by the applicability of the diffusion limit, but also by the assumption of a quasi-steady stochastic process, which is clearly invalid during the first few hundred Myr, which are characterised by a highly evolving phase, involving the initial gas contraction and the triggering of a starburst that expels most of it out of  $r_s$ .

Assuming  $v_r \approx 30 \text{ kpc/Gyr}$ , gives  $(v_r k_m)^{-1} \lesssim 1/30 \text{ Gyr}$ , for  $1/k_m \lesssim 1 \text{ kpc}$ . Thus the steady state diffusion limit may be safely assumed to be established beyond 1 Gyr. We will take it to be our zero point for  $T = t - t_{\text{diff}}$ .

As in standard two body relaxation, one may assume that fluctuations initially change just the velocities of the halo particles<sup>5</sup>

<sup>5</sup> This is strictly speaking valid when the orbital period of halo particles  $T_p$  is much longer than the fluctuation timescale  $T_f$ . Here, they are generally of the same order. However the impulsive approximation is known to remain reasonable even when  $T_p$  is moderately smaller than  $T_f$  (e.g. Binney & Tremaine 2008; Aguilar & White 1985; Peñarrubia 2019a). For a circular orbit and gas mode of wavenumber  $k$ ,  $T_p/T_f = kr v_r/v_c(r)$ . This is minimized in the initial cuspy potential, and when  $k = k_m$ , and  $v_r \approx 30 \text{ km/s}$  includes only the gas speed. For  $k_m = 2 \text{ kpc}^{-1}$  (consistent with Fig. 4), this minimal ratio is  $T_p/T_f \approx 3$  for  $r \approx 1 \text{ kpc}$ . It is significantly smaller than unity ( $\lesssim 1/3$ )

The average energy change per unit mass resulting from this is  $\langle \Delta E \rangle = \langle \Delta \frac{1}{2} (\Delta v)^2 \rangle = v \langle \Delta v \rangle + \frac{1}{2} \langle (\Delta v)^2 \rangle$ . In principle, the particles may gain energy through the first term or lose it to the fluctuating field through dynamical friction, as in any general diffusive dynamical process. But in practice the mass of the particles is far too small and so the average energy gain per unit mass is simply  $\langle \Delta E \rangle = \frac{1}{2} \langle (\Delta v)^2 \rangle$ .

By fixing  $v_r$ , and assuming the energy transfer mechanism to be global — again, in the sense of depending on an effective characteristic density  $\rho_0$  rather than on the local  $\langle \rho_g \rangle_T(r)$  — the expected energy input to halo particles within radius  $r$  may be estimated as

$$E_{\text{in}}(< r) = \langle M(< r) \rangle \langle \Delta E \rangle = \langle M(< r) \rangle \frac{4\pi(G\rho_0)^2 \mathcal{P}_{k_m} T}{nv_r}, \quad (6)$$

where  $\langle M(< r) \rangle$  is the (time) average of the halo mass enclosed within  $r$ .

We discuss the assumption of global energy input below. First, we assume it holds at least approximately, and use it to estimate the total energy transfer from the gas to the halo. Given the rapidly decreasing gas density beyond  $r_s$  (Fig. 3), one may suppose that the energy input saturates at  $r_{\text{sat}} \gtrsim r_s$ . If the energy transfer depends on global properties, then  $\rho_0$  may be considered to correspond to the space and time average of the gas density inside  $r_{\text{sat}}$ , i.e.  $\rho_0(\text{sat}) = \langle \rho_0(r_{\text{sat}}, t) \rangle_T$ , where  $\rho_0(r_{\text{sat}}, t)$  is given by (3), with  $r = r_{\text{sat}}$  (unless otherwise stated, particularly in relation to Fig. 8, time averages are evaluated from  $T = 0$ , i.e.  $t = t_{\text{diff}} = 1 \text{ Gyr}$ , to the end of the simulation at  $t = 13.7 \text{ Gyr}$ ). For  $r_{\text{sat}} \gtrsim r_s$ ,  $\langle M(< r) \rangle$  is close to the initial mass at  $T = 0$ , since the dark matter mass inside it is essentially conserved. We thus write, in terms of the initial mass  $M_0(< r)$ ,

$$E_{\text{in}}(< r_{\text{sat}}) = 10^9 M_\odot \text{ kpc}^2 \text{ Gyr}^{-2} \frac{M_0(< r_{\text{sat}})}{10^8 M_\odot} \frac{T}{\text{Gyr}} \times \left(\frac{n}{2.5}\right)^{-1} \left(\frac{v_r}{30 \text{ km/s}}\right)^{-1} \left(\frac{\mathcal{P}(k_m)}{3 \text{ kpc}^3}\right) \left(\frac{\rho_0(r_{\text{sat}})}{10^6 M_\odot \text{ kpc}^{-3}}\right)^2, \quad (7)$$

where we have chosen  $v_r$  in accordance with the discussion of the previous subsection, and inserted values characteristic of the initial halo mass and average gas density (as defined above) around  $r_s$ . More precisely, the numbers correspond to values at  $r = r_{\text{sat}} = 1.5 r_s \approx 1.3 \text{ kpc}$ , but we note that the estimate of the total energy input is not sensitive to the choice of  $r_{\text{sat}}$ ; as the product  $M_0(< r) \rho_0^2(r)$  varies slowly with radius around  $r_s$  (indeed, more generally,  $\langle M(< r) \rangle \rho_0^2(r)$  varies by at most a factor of 2 in the range  $0.1 r_s \leq r \leq 2 r_s$ ). The power spectrum parameters are estimated from the results in figures 4 and 6 (a larger  $\mathcal{P}(k_m) = 4 \text{ kpc}^3$  gives the same result if  $v_r = 40 \text{ km/s}$ , which would take into account enhancement in the speeds of halo halo particles, relative to the gas, due to their own motion).

We now wish to compare the prediction in equation (7) with the actual energy input inferred from the simulation. For this purpose, we define the quantity

$$E_r = \frac{m}{2} \left( \sum_i v_i^2 + \Phi_i \right), \quad (8)$$

where  $m$  is the halo particle mass in the simulation,  $v_i$  is the speed of particle  $i$  and  $\Phi_i$  is the Newtonian potential at its location. The summation is evaluated over all particles within radius  $r$ . Increase

only at  $r < 30 \text{ pc}$ . Adiabatic corrections may be included (Peñarrubia 2019a), though the corrections are generally modest for our range of  $T_p/T_f$  (Cf. Fig. 2 of Peñarrubia 2019a). In our context the impulsive regime also in fact places a lower limit on  $k_m$ , independent of the flattening of the power spectrum in Fig. 4, as the effect of fluctuations rapidly decreases beyond it.



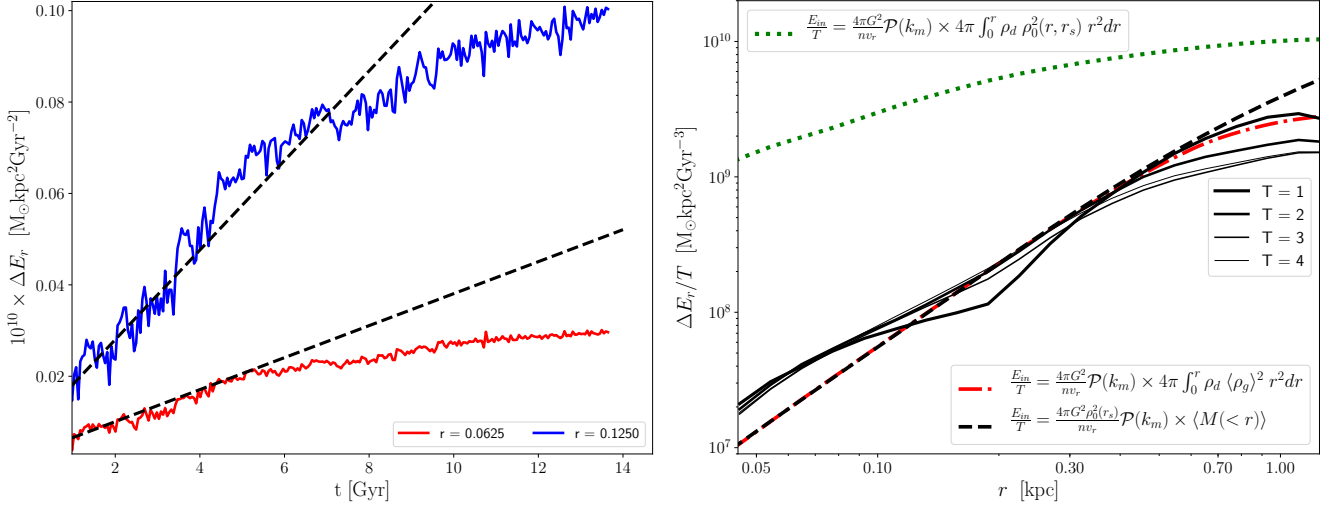


**Figure 8.** Local vs global energy transfer. *Left:* Radial energy transfer as a function of time. *Right:* Energy input rate as a function of radius. The left hand panel shows that radial energy transfer is slow compared to the energy input; the straight lines represent steady diffusive energy input, with no transfer outside the radii enclosed. While this holds, one may estimate the energy input rate at various radii by simply evaluating the average slope of the generally linear energy increase. The right hand panel shows those slopes over the first 1, 2, 3 and 4 Gyr (solid lines with indicated values of  $T$ ). The dashed line corresponds to estimate assuming global energy transfer; using equation (6) with  $n = 2.5$ ,  $v_r = 30.0$  km/s,  $\mathcal{P}(k_m) = 3.6$  kpc<sup>3</sup>, and average gas density within  $r_s$ ,  $\rho_0(r_s) = \langle \rho_0(r_s, t) \rangle_T$ , with  $\rho(r, t)$  measured directly from the simulation (using equation 3) and averaged over  $T = [0 : 4]$  Gyr (giving  $\rho_0 = 1.95 \times 10^6$  M<sub>⊙</sub>/kpc<sup>3</sup>). The dotted line corresponds to the assumption of purely local energy input; using the indicated equation, where the local gas density  $\rho_g(\mathbf{r}, t)$  is time-averaged (in the range  $T = [0 : 4]$  Gyr) over spherical shells at  $r$ . This vastly overestimates the energy input at all radii. The dashed dotted line represents an intermediate alternative, whereby  $\rho_g$  is averaged over spheres of radius  $r_s$  and centered at  $r$  (as in equation 9).

in this quantity measures the energy input inside radius  $r$ , provided there is no dark matter mass or energy outflow from that radius and the mass distribution beyond it remains constant (so that changes in the potential are solely due to modification of the mass distribution within  $r$ )<sup>6</sup>. We may expect that these conditions hold, at all radii, for sufficiently small times, as the kinetic energy acquired by the halo particles is still being converted into changes in the mass distribution and potential, a process slower than that characterising the initial energy input. The conditions should hold for longer times as  $r$  increases; and we expect that beyond  $r_{\text{sat}} \gtrsim r_s$ , the energy input saturates to a specific value regardless of radius, and little energy is transferred beyond that radius, so the change in  $E_r$  from its initial value (at  $T = 0$ ) corresponds to the total energy input from the fluctuating gas. In particular, if that input may be estimated theoretically using equation (7), then one expects  $\Delta E_{r_{\text{sat}}} \approx E_{\text{in}}(< r_{\text{sat}})$ .

These expectations are confirmed in Fig. 7. At all radii, we initially find a general linear increase in  $E_r$ , as expected from a steady diffusive process, with stochastic variations on this general trend. At smaller radii, the lines clearly flatten after a few Gyr, as a result of energy and mass outflow onto larger  $r$ . A saturation radius  $r_{\text{sat}} \gtrsim r_s$ , beyond which the lines converge, can be defined with value consistent with  $r_{\text{sat}} = 1.5 r_s \approx 1.3$  kpc as assumed in equation (7). The slope derived from that relation is also consistent with that derived directly from the simulation, as indicated by the dashed line.

The above suggests that the total energy input within  $r_{\text{sat}}$  may be adequately described by assuming a global energy transfer mechanism, parameterised by the average gas density and halo mass at  $r_{\text{sat}}$  inferred from the simulation; and with  $v_r$  and density contrast

power spectrum parameters also consistent with those found in the simulated hydrodynamics.

We now wish to ask to what extent this global approximation holds in general; for, as the time averaged gas density inside  $r_s$  is not strictly constant, energy transfer may, in principle, depend instead on the local density. This is a possibility akin to invoking the purely local approximation when evaluating the effect of two body relaxation in stellar dynamics, by using Chandrasekhar’s formula and plugging in the local stellar density. This is in principle plausible, but more difficult to interpret in the present case; whereas in two body relaxation logarithmic intervals in impact parameters (or spatial scales) equally contribute to the fluctuations leading to relaxation, here fluctuations at the largest scales (characterized by  $\mathcal{P}(k_m)$ ) are more important.

Global energy transfer implies the validity of equation (6). Local energy transfer, on the other hand, requires the evaluation of the time average  $\langle \rho_g(r, t) \rangle^2(r)$  over spherical shells centered at  $r$ , and integrating it over the dark matter mass in those shells,  $4\pi r^2 \rho_d(r)$  (assuming a fixed  $v_r$ ). The right panel of Fig. 8 (dotted line) shows that, when assuming power spectrum parameters and velocity  $v_r$  consistent with the simulation, this vastly overestimates the energy input. The non-local assumption — with energy input rate within radius  $r$  scaling simply as  $\rho_0^2 M(< r)$  as implied by equation (6) — results in much better agreement, with a moderate discrepancy at small radii that may at least partly be accounted for by an increase of  $v_r$  with radius (as discussed above and expected from Fig. A4), which we do not take into account here for simplicity.

The global approximation, with total energy input within radius  $r$  simply proportional to  $M(< r)$ , clearly cannot remain valid as  $r \rightarrow r_{\text{sat}}$ , when the gas density and fluctuations rapidly decrease. Indeed, the difference between  $\rho_0(r_s)$  that fits the energy transfer rate in Fig. 8 and  $\rho_0(r_{\text{sat}})$  used in Fig. 7, principally reflects the gradual saturation process; the fit in Fig. 7 effectively assumes sudden

<sup>6</sup> The potential  $\Phi_i$  at particle  $i$  is due to other halo particles; we ignore changes in the potential arising directly from the gas flows, as these constitute a fluctuating contribution with small average, particularly after the initial expulsion episode during the first few hundred Myr

saturation, while in reality the process is gradual. To take this into account one may invoke an intermediate regime, between the purely local and purely global energy transfer limits. We do this by defining

$$\rho_0(r, r_{\text{av}}) = \langle \rho_g(\mathbf{r}, \mathbf{r} - \mathbf{r}_g) \rangle_{r, |\mathbf{r} - \mathbf{r}_g| < r_{\text{av}}, T}, \quad (9)$$

where the average over the gas density is evaluated over time at points  $\mathbf{r}_g$  inside spheres with centres at radial coordinate  $r$  and radii  $r_{\text{av}}$ . Thus in this context,  $\rho_0(r_{\text{sat}}) = \rho_0(0, r_{\text{sat}})$  and  $\rho_0(r_s) = \rho_0(0, r_s)$ . The results for  $\rho_0(r, r_s)$  are shown by the dashed dotted line in the right hand panel of Fig. 8. They suggest that the energy transfer process is best considered as non-local, with a range  $\sim r_s$ .

Finally, we note that although the energy is assumed to be transferred to halo particles initially as kinetic energy, due to modification in their velocities (as given by equation 5), the changes eventually affect the self consistent potential. The resulting average gain in total energy per unit mass turns out to be amenable to estimation from a low energy cutoff that appears in the phase space distribution function. In Appendix B, we show how this can be related to the energy input calculated here, and connected to the change in the potential that accompanies core formation.

### 4.3 Mass migration and core formation

The energy input from the fluctuating gas leads to the migration of halo particles from the inner radii, which decreases the enclosed mass, as shown in Fig. 9, left panel. Straight lines on the log linear scale suggest a general exponential decrease in mass with time. A full examination of its origin in the context of a diffusion model would require a full Fokker Planck formulation, using the full (first and second order) diffusion coefficients and explicitly including changes in the potential due to the evolving mass distribution. Here we proceed heuristically, leaving the examination of the reasons why the drastic simplifications invoked seem to work to Appendix C.

We suppose that the mass flux across energy surface  $E$  changes the mass within it through the first order energy diffusion coefficient

$$D[\Delta E] = \frac{1}{M(< r_{\text{sat}})} \frac{E_{\text{in}}(r_{\text{sat}})}{T}, \quad (10)$$

describing the average rate of change of halo particle energy per unit mass due the gas fluctuations. At the energy input rate inferred from Fig. 7, this is of the order of  $10 \text{ kpc}^2 \text{ Gyr}^{-3}$  in the simulation at hand (which is consistent with theoretical expectations, given the power spectrum and density inferred from simulation, cf. equation 7, but is actually empirically independent of the model).

The change in mass of particles with energy less than  $E$  is

$$\frac{\partial M(< E)}{\partial t} \approx - \frac{\partial M(< E)}{\partial E} D[\Delta E], \quad (11)$$

where  $M(< E)$  is the mass in halo particles with energy less than  $E$  and  $\partial M(< E)/\partial E$  is the mass-weighted differential energy distribution (Binney & Tremaine 2008). Furthermore, we approximate this latter quantity by its average within  $E$ , such that

$$\frac{\partial M(< E)}{\partial E} \approx a_p \frac{M(< E) - M(0)}{E - E(0)}, \quad (12)$$

where  $E(0)$  is the energy of a particle at rest at the centre of the potential (so  $E(0) = \Phi(0)$  and  $M(0) = 0$ ), and  $a_p$  is a constant numerical factor of order 1. This holds exactly inside pure power-law cusps: e.g. as derived in Appendix C, one finds in such cases that  $a_p = (3 + \gamma)/(2 + \gamma)$  for  $\rho \propto r^{-\gamma}$  (thus  $a_p = 2$  for a  $1/r$  cusp, tends towards 1.5 for flatter profiles, and is larger for steeper ones

(finally diverging in the case of the singular isothermal sphere, where a potential zero point at the centre cannot be fixed as above due to logarithmic divergence).

With this in mind we will assume that

$$\frac{\partial M(< E)}{\partial t} = -a \frac{M(< E) - M(0)}{E - E(0)} D[\Delta E], \quad (13)$$

where the parameter  $a$  absorbs all of the major approximations involving the use of the first order diffusion coefficient (equation 11), the association of the differential energy distribution with its average value (equation 12), and the neglect of the effect of the evolution of the self consistent potential.

In Appendix C, we discuss how such a formulation may be justified if the differential energy distribution may be approximated by a power law; and how, when one includes both diffusion coefficients, a zero Fokker Planck flux may be attained if the distribution takes an exponential form.

We now define an energy relaxation time as

$$t_{\text{relax}}(E) = D[\Delta E]^{-1} [E - E(0)]. \quad (14)$$

For timescales small compared to the initial relaxation time (with  $E$  and  $E_0$  defined at the initial time), one may take this timescale to be constant, evaluated by inserting the initial values of  $E$  and  $E_0$  in the above equation. We will assume that this is the case here (as we will see below, the energy changes are small enough, during timescales of interest, to render this approximation reasonable). Then, assuming that equation (11) is applicable in the diffusion limit, solving it (starting at time  $T = 0$ ) results in

$$M(< E) = M_0(< E) \exp[-a T/t_{\text{relax}}(E)], \quad (15)$$

where  $M_0$  refers to the mass at time  $T = 0$ .

Within this picture, the numbers on the lines in the left panel of Fig. 9, denoted by  $\alpha$ , should correspond to  $a/t_{\text{relax}}(E)$ , if  $E$  is associated with particle energies inside the chosen radii. To make this correspondence, we fix  $E = \langle E \rangle(r)$  to be the average specific energy at radius  $r$  in the initial profile. As a first approximation, we simply associate this with the initial NFW profile of the configuration. The specific potential energy  $\Phi(r) - \Phi(0)$  in this case is  $4\pi G \rho_s r_s^2 [1 - \ln(1+x)/x]$ , with  $x = r/r_s$ , and  $r_s$  and  $\rho_s$  as in Table 1. To obtain a simple form for the kinetic energy we make use of established empirical relations according to which the pseudo phase space density varies with radius approximately as  $\rho/\langle v^2 \rangle^{3/2} \sim r^{-1.875}$  (Taylor & Navarro 2001), and normalize the velocity variance to its value around  $r = r_s$ , such that  $\langle v^2 \rangle \approx 470 \text{ km}^2/\text{s}^2$ . One may then write

$$E - E(0) \approx 4\pi G \rho_s r_s^2 \left[ 1 + \frac{2^{4/3}}{10} \frac{(x^{0.875})^{2/3}}{(1+x)^{4/3}} - \frac{\ln(1+x)}{x} \right]. \quad (16)$$

Using this formula in conjunction with equation (14), and using  $a = 3.4$ , we find  $a/t_{\text{relax}} = 0.034, 0.047, 0.071, 0.11, 0.17 \text{ Gyr}^{-1}$  at  $r = 1, 0.5, 0.25, 0.125, 0.0625 \text{ kpc}$  respectively. These numbers agree to better than 20% with the values of  $\alpha$  indicated on the fitting lines in Fig. 9 (left panel). The corresponding energy relaxation times are about 100, 72.3, 47.9, 30.9 and 20 Gyr.

A more careful analysis, taking into account that the quasi-steady state diffusive process is well established only after  $t \gtrsim t_{\text{diff}} = 1 \text{ Gyr}$ , suggests  $a \approx 2.5$  (cf. below). The corresponding energy relaxation times are therefore lower by a factor of about 1.4 than those quoted above. Even then, these relaxation times are still significantly larger than what is obtained from the velocity variance (equation 4). This is because  $E - E(0)$  is generally larger than the average kinetic energy

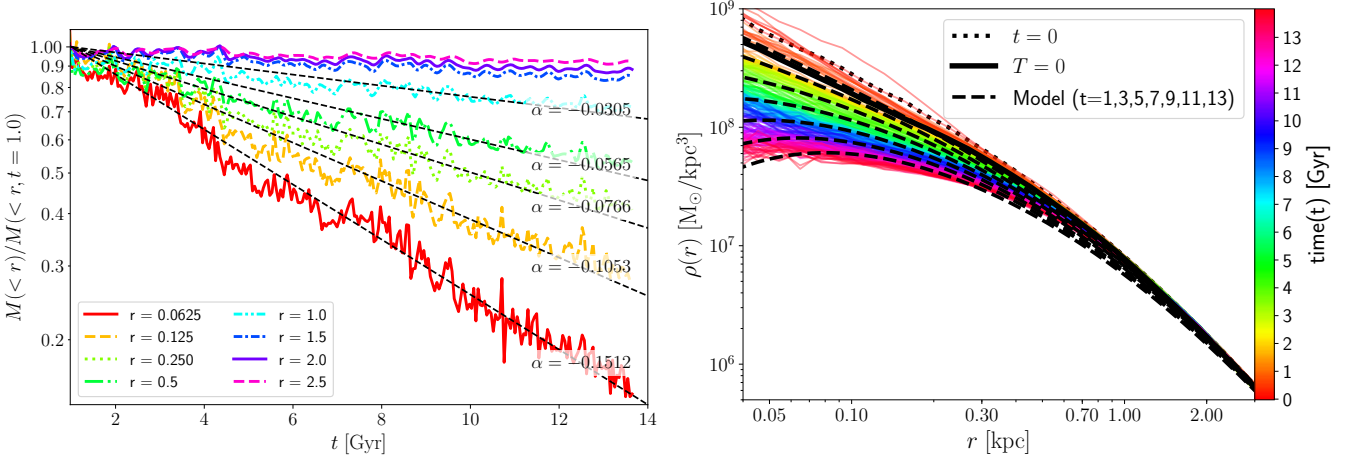


**Figure 9.** Mass migration and core formation. The left panel shows the ratio between the halo mass within radii  $r$  (in kpc) and the corresponding initial mass at  $T = 0$  ( $t = t_{\text{diff}} = 1$  Gyr, as discussed in relation to Fig. 7). The dashed lines are exponential fits,  $\propto \exp(\alpha T)$ , with numbers corresponding to  $\alpha(r)$  in  $\text{Gyr}^{-1}$ . The exponential decay may be derived from a simple theoretical model for the mass transfer; in its context  $\alpha$  is predicted to scale with the inverse of an energy relaxation time (obtained using Eqs. 14, 10, and 16). The right panel shows the corresponding evolution in density. Theoretical expectations are shown by the dashed lines. They are obtained by differentiating equation (15), starting from an NFW fit to the dark matter density in the simulation at  $T = 0$ . To reduce uncertainties arising from fluctuations in the density profile around  $T = 0$ , we average simulation outputs over the range  $0.5 \text{ Gyr} \leq t \leq 1.5 \text{ Gyr}$  (as in Fig. 7). Model predictions are shown at  $T = 0$  (fitting the averaged profile), and at 2, 4, 6, 8, 10 and 12 Gyr, corresponding to times 1, 3, 5, 7, 9, 11 and 13 Gyr.

(from equation 16, by a factor of about four at  $r_s$ ). Indeed, changes in kinetic energy lead to relatively little change in total energy. In fact the relative change in  $E_r$  at 1 kpc (as calculated from equation 8, starting at  $T = 0$ ), is  $\Delta E_r/E_r \approx 0.2$ , over 12.7 Gyr. Initially the rate of relative change in energy is much larger at smaller radii (as illustrated by the differences in  $E_{\text{in}}/T$  inferred from Figs. 7 and 8). But it subsequently saturates, as the energy is redistributed in the system, with mass and energy flowing towards outer radii (Fig. 8, left panel). When thus redistributed, the modest changes in total energy lead to a modification of the self consistent potential, including the minimal possible energy in it, as discussed in Appendix B.

This leads to core formation, as observed in the right panel of Fig. 9. There, we note that we find no evidence of any accelerated core formation, relative to the velocity relaxation time (equation 4), as found in El-Zant et al. (2016), when non-spherical modes were used in conjunction with the Hernquist-Ostriker code.

Having obtained the evolution of the enclosed mass within a given radius, it is also possible to define a theoretical density  $\rho = r^{-2} dM/dr$  and derive a closed form formula for it using Eqs. (15), (14), and (16). The result may then be compared with the dark matter density evolution in the simulation. More care is however required here in defining the initial energies in equation (16), as we must start our comparison at  $T = t - t_{\text{diff}} = 0$ , i.e., when the diffusion limit at the basis of our model is valid (cf. the discussion in relation to Fig. 7). For this purpose, we average simulation outputs in the time range  $0.5 \text{ Gyr} \leq t \leq 1.5 \text{ Gyr}$ , and then fit the resulting dark matter density with an NFW profile. The corresponding parameters are  $r_s = 1.17 \text{ kpc}$  and  $\rho_s = 2.7 \times 10^7 M_\odot/\text{kpc}^3$ . When the latter is adjusted by adding a gas fraction of about 0.075 (assumed for simplicity to be also NFW with same  $r_s$ , but taking into account the initial central gas expulsion), the multiplicative factor  $\rho_s r_s^2$  in front of the bracket in equation (16) remains approximately the same as in the case of the  $t = 0$  profile. After some trials, we found that values of  $a$  in the range 2.5 to 2.8 provide reasonable approximations to the density evolution inferred from the simulation (perhaps surprisingly so, given the various simplifying assumptions of our mass transfer model). This is illustrated in the right panel of Fig. 9, where we com-

pare the density evolution expected from our model (fixing  $a = 2.5$ ) with the results from the simulation.

Note that, other than the value of  $a$ , which is theoretically fairly tightly constrained by the arguments of Appendix C (cf. equation C14), there are no free parameters in these fits. The energy distribution of halo particles at  $T = 0$ , and the energy transfer rates from gas to halo, are of course characteristic of a given system. They will thus vary from simulation to another, but they are entirely fixed for any one system (within numerical uncertainties in their inference from the simulation).

## 5 CONCLUSION

Potential fluctuations from feedback driven gas can ‘heat’ halo cusps, turning them into cores. This work aimed at quantifying this, by measuring the gas fluctuations and tracking the way they transfer energy to the central halo, forcing the outward migration of the dark matter. The interpretive framework we use is a model, first outlined in El-Zant et al. (2016), which predicts that these processes principally depend on the amplitude of the fluctuations, as measured by the normalisation of their power spectrum, and the average gas density. The result being a standard diffusion process, characterised by a linear temporal increase in velocity variance and energy of halo particles as a result of their interaction with the fluctuating gas field. As shown previously (El-Zant et al. 2020), in this picture the effect of the fluctuations reduces to standard two body relaxation in the case of a white noise power spectrum. It may thus, in this limit, also describe halo heating *via* dynamical friction from a system of compact, monolithic massive clumps moving among much lighter dark matter particles.

To test this interpretive framework, we measure the density fluctuations in feedback-driven gas from a full hydrodynamic simulation of a model dwarf galaxy (Figs. 1-3), and obtain their density contrast power spectrum (Fig. 4). We find that the spectrum follows a power-law in wave number ( $\propto k^{-n}$ ), with an exponent  $2 \leq n \leq 3$ , for the whole period of the simulation (spanning a Hubble time). Although

the time-averaged density of the driven gas varies with radius, the variation is modest inside the initial NFW scale length, relative to a sharp drop outside. This suggests a characteristic density that may be used as input for the model. We also examine the velocity distribution of the gas and find that it is approximately fit by Maxwellians at larger radii (Appendix A). The kinetic energy power spectrum is close to the Kolmogorov form over large range of scales (Fig. 5). This reinforces the picture of a fully turbulent medium.

With the input parameters directly measured from the simulation, we use our model to calculate the total energy transfer rate from fluctuating gas to the central halo. The result is compared with the actual energy input to the system of halo particles, as directly inferred from the simulation (Fig. 7). This is found to generally agree — displaying the general linear increase, expected of a steady diffusion process — over almost a Hubble time. We also examine the radial distribution of the energy input rate (Fig. 8). We find that the energy transfer is indeed much better approximated as a global rather than local process; in the sense that it depends on the average gas energy density within the core region rather than the local density at each radius.

The energy is initially transferred from the gas as kinetic energy to individual halo particles, but it is then redistributed through the self consistent gravity of the system, a process through which the core replaces the cusp. The process comes with a low energy cutoff in the halo phase space distribution function, as particles migrate to higher energy levels. It is straightforward to link the level of this cutoff to the total energy input from the gas, and to the resulting change in halo gravitational potential that comes with core formation (Appendix B).

The energy flow upwards is accompanied by a mass flow outwards. We empirically find an exponential decrease in halo mass with time, within a given radius, in the initial cusp. We then devise a simple approximate description of the mass flow, based on our model, from which the exponential form may be inferred. In this context, the exponential decay time scales with (and is of the order of) the local (energy) relaxation time, and the evolution of the corresponding theoretical density profile mimics that in the simulation (Fig. 9).

Strictly speaking, energy transfer *via* a standard diffusion process requires the gas force fluctuations to be normally distributed. We have verified this to be the case to a good approximation (even if the larger *density* fluctuations can be lognormal rather than Gaussian at small radii, cf. Appendix A). Another assumption of the model is the use of the ‘sweeping’ approximations of turbulence theory, whereby the statistics of the spatial fluctuations are transferred to the time domain through large scale flows. The general consistency of the spatial power spectrum parameters with those that fit the mass dispersion in the time domain (Fig. 6), confirm that this may be an applicable approximation.

In general, the assumptions and predictions of the theoretical framework seem vindicated for the model galaxy studied here. This suggests a remarkably concise description of halo core formation from gaseous fluctuations, summarizing the effect of much complex ‘gastrophysics’ in terms of the two principal parameters of gas density and fluctuation levels. Obvious extensions include considering different galaxy masses, as well as verifying that the model also predicts a lack of core formation in simulations that do not produce them. Success there would help delineate particular elements in the physical ‘subgrid’ input that are most crucial in producing the required conditions for core formation, and examining how they compare with observations.

It may also be possible to test the predictions regarding the level of the fluctuations required for core formation directly from observations. In particular, it has already been possible to derive surface

density power spectra for larger, and relatively quiescent galaxies. Estimating these for actively star forming galaxies, and calibrating them with three dimensional density contrast power spectra entering into our model calculations, may provide a direct test of our picture of core formation through gaseous fluctuations.

## ACKNOWLEDGEMENTS

We would like to thank the referee for a careful reading, thorough report and constructive criticism that helped improve our manuscript.

## DATA AVAILABILITY

The simulation data underlying this article will be shared on reasonable request.

## REFERENCES

- Agertz O., Kravtsov A. V., Leitner S. N., Gnedin N. Y., 2013, *ApJ*, **770**, 25  
Aguilar L. A., White S. D. M., 1985, *ApJ*, **295**, 374  
Bar-Or B., Kupi G., Alexander T., 2013, *ApJ*, **764**, 52  
Bar N., Blum K., Sun C., 2021, arXiv e-prints, p. arXiv:2111.03070  
Binney J., Tremaine S., 2008, *Galactic dynamics*  
Bouché N. F., et al., 2022, *A&A*, **658**, A76  
Boylan-Kolchin M., Bullock J. S., Kaplinghat M., 2011, *MNRAS*, **415**, L40  
Bullock J. S., Boylan-Kolchin M., 2017, *Annual Review of Astronomy and Astrophysics*, **55**, 343  
Burkert A., 2000, *ApJ*, **534**, L143  
Burkert A., 2020, arXiv e-prints, p. arXiv:2006.11111  
Coles P., Jones B., 1991, *MNRAS*, **248**, 1  
Collins M. L. M., Read J. I., 2022, *Nature Astronomy*, **6**, 647  
Dekel A., et al., 2021, *MNRAS*, **508**, 999  
Del Popolo A., Le Delliou M., 2017, *Galaxies*, **5**, 17  
Deng H., Hertzberg M. P., Namjoo M. H., Masoumi A., 2018, *Phys. Rev. D*, **98**, 023513  
Di Cintio A., Brook C. B., Macciò A. V., Stinson G. S., Knebe A., Dutton A. A., Wadsley J., 2014, *MNRAS*, **437**, 415  
Dubinski J., Carlberg R. G., 1991, *ApJ*, **378**, 496  
El-Zant A. A., 2008, *ApJ*, **681**, 1058  
El-Zant A., Shlosman I., Hoffman Y., 2001, *ApJ*, **560**, 636  
El-Zant A. A., Hoffman Y., Primack J., Combes F., Shlosman I., 2004, *ApJ*, **607**, L75  
El-Zant A. A., Freundlich J., Combes F., 2016, *MNRAS*, **461**, 1745  
El-Zant A. A., Freundlich J., Combes F., Halle A., 2020, *MNRAS*, **492**, 877  
Errani R., Navarro J. F., Peñarrubia J., Famaey B., Ibata R., 2023, *MNRAS*, **519**, 384  
Evans N. W., 1994, *MNRAS*, **267**, 333  
Falkovich G., 1994, *Physics of Fluids*, **6**, 1411  
Famaey B., Khoury J., Penco R., Sharma A., 2020, *J. Cosmology Astropart. Phys.*, **2020**, 025  
Flores R. A., Primack J. R., 1994, *ApJ*, **427**, L1  
Frenk C. S., White S. D. M., 2012, *Annalen der Physik*, **524**, 507  
Freundlich J., Dekel A., Jiang F., Ishai G., Cornuault N., Lapiner S., Dutton A. A., Macciò A. V., 2020a, *MNRAS*, **491**, 4523  
Freundlich J., et al., 2020b, *MNRAS*, **499**, 2912  
Gilman D., Birrer S., Nierenberg A., Treu T., Du X., Benson A., 2020, *MNRAS*, **491**, 6077  
Governato F., et al., 2015, *MNRAS*, **448**, 792  
Grisdale K., Agertz O., Romeo A. B., Renaud F., Read J. I., 2017, *MNRAS*, **466**, 1093  
Hernquist L., Ostriker J. P., 1992, *ApJ*, **386**, 375  
Inoue S., Dekel A., Mandelker N., Ceverino D., Bournaud F., Primack J., 2016, *MNRAS*, **456**, 2052  
Iršič V., et al., 2017a, *Phys. Rev. D*, **96**, 023522

- Iršič V., Viel M., Haehnelt M. G., Bolton J. S., Becker G. D., 2017b, *Phys. Rev. Lett.*, **119**, 031302  
 Kim S. Y., Peter A. H. G., Hargis J. R., 2018, *Phys. Rev. Lett.*, **121**, 211302  
 Kochanek C. S., White M., 2000, *ApJ*, **543**, 514  
 Kogosov S., et al., 2008, *ApJ*, **686**, 279  
 Kraichnan R. H., 1964, *Physics of Fluids*, **7**, 1723  
 Kritsuk A. G., Norman M. L., Padoan P., Wagner R., 2007, *ApJ*, **665**, 416  
 Li Z., Dekel A., Mandelker N., Freundlich J., François T., 2022, arXiv e-prints, p. arXiv:2206.07069  
 Macciò A. V., Paduroiu S., Anderhalden D., Schneider A., Moore B., 2012, *MNRAS*, **424**, 1105  
 Moore B., 1994, *New Astron.t*, **370**, 629  
 Nadler E. O., et al., 2020, arXiv e-prints, p. arXiv:2008.00022  
 Nadler E. O., Birrer S., Gilman D., Wechsler R. H., Du X., Benson A., Nierenberg A. M., Treu T., 2021, *ApJ*, **917**, 7  
 Navarro J. F., Eke V. R., Frenk C. S., 1996a, *MNRAS*, **283**, L72  
 Navarro J. F., Frenk C. S., White S. D. M., 1996b, *ApJ*, **462**, 563  
 Newton O., et al., 2021, *J. Cosmology Astropart. Phys.*, **2021**, 062  
 Nusser A., Silk J., 2022, *MNRAS*, **509**, 2979  
 Ogiya G., Burkert A., 2015, *MNRAS*, **446**, 2363  
 Ogiya G., Nagai D., 2022, *MNRAS*, **514**, 555  
 Oman K. A., Marasco A., Navarro J. F., Frenk C. S., Schaye J., Benítez-Llambay A., 2019, *MNRAS*, **482**, 821  
 Orkney M. D. A., et al., 2021, *MNRAS*, **504**, 3509  
 Peñarrubia J., 2019a, *MNRAS*, **484**, 5409  
 Peñarrubia J., 2019b, *MNRAS*, **490**, 1044  
 Peñarrubia J., Pontzen A., Walker M. G., Kogosov S. E., 2012, *ApJ*, **759**, L42  
 Pontzen A., Governato F., 2014, *Nature*, **506**, 171  
 Read J. I., Erkal D., 2019, *MNRAS*, **487**, 5799  
 Read J. I., Gilmore G., 2005, *MNRAS*, **356**, 107  
 Read J. I., Trentham N., 2005, *Philosophical Transactions of the Royal Society of London Series A*, **363**, 2693  
 Read J. I., Wilkinson M. I., Evans N. W., Gilmore G., Kleya J. T., 2006, *MNRAS*, **367**, 387  
 Read J. I., Agertz O., Collins M. L. M., 2016, *MNRAS*, **459**, 2573  
 Read J. I., Walker M. G., Steger P., 2019, *MNRAS*, **484**, 1401  
 Salucci P., 2019, *Astron. Astrophys. Rev.*, **27**, 2  
 Salucci P., Turini N., di Paolo C., 2020, *Universe*, **6**, 118  
 Schmidt W., Hillebrandt W., Niemeyer J. C., 2004, arXiv e-prints, pp astro-ph/0407616  
 Simon J. D., Geha M., 2007, *ApJ*, **670**, 313  
 Spitzer L., 1987, Dynamical evolution of globular clusters  
 Taylor G. I., 1938, *Proceedings of the Royal Society of London Series A*, **164**, 476  
 Taylor J. E., Navarro J. F., 2001, *ApJ*, **563**, 483  
 Tennekes H., 1975, *Journal of Fluid Mechanics*, **67**, 561  
 Teyssier R., 2002, *A&A*, **385**, 337  
 Teyssier R., Pontzen A., Dubois Y., Read J. I., 2013, *MNRAS*, **429**, 3068  
 Turner H. C., Lovell M. R., Zavala J., Vogelsberger M., 2021, *MNRAS*, **505**, 5327  
 Warren M. S., Quinn P. J., Salmon J. K., Zurek W. H., 1992, *ApJ*, **399**, 405  
 Widrow L. M., 2000, *ApJS*, **131**, 39  
 Yang D., Nadler E. O., Yu H.-b., 2022, arXiv e-prints, p. arXiv:2211.13768  
 Yu X., Bian F., Krumholz M. R., Shi Y., Li S., Chen J., 2021, *MNRAS*, **505**, 5075

## APPENDIX A: STATISTICS OF THE GAS FLUCTUATIONS

For the description of the effect of the gas fluctuations on the halo particles in terms of a diffusion process, leading to relaxation timescales of the form of Eq (2), to be complete, their statistics should be entirely described by averages and dispersions, as in a Gaussian random process. We wish to examine whether this is the case with the gas fluctuations considered in this work.

Fig. A1 shows the statistics of the mass fluctuations in three different bins in the region where the core forms. For  $r \gtrsim 0.5r_s$  the

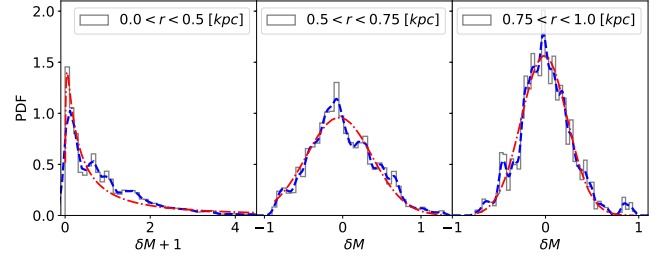


**Figure A1.** Probability distribution function (PDF) of the mass fluctuations within different radii  $r$ . The fluctuations are well-fit by Gaussians for  $r \geq 0.50.5\text{kpc}$  and by a lognormal distribution below. The fits are shown by the red dashed-dotted lines

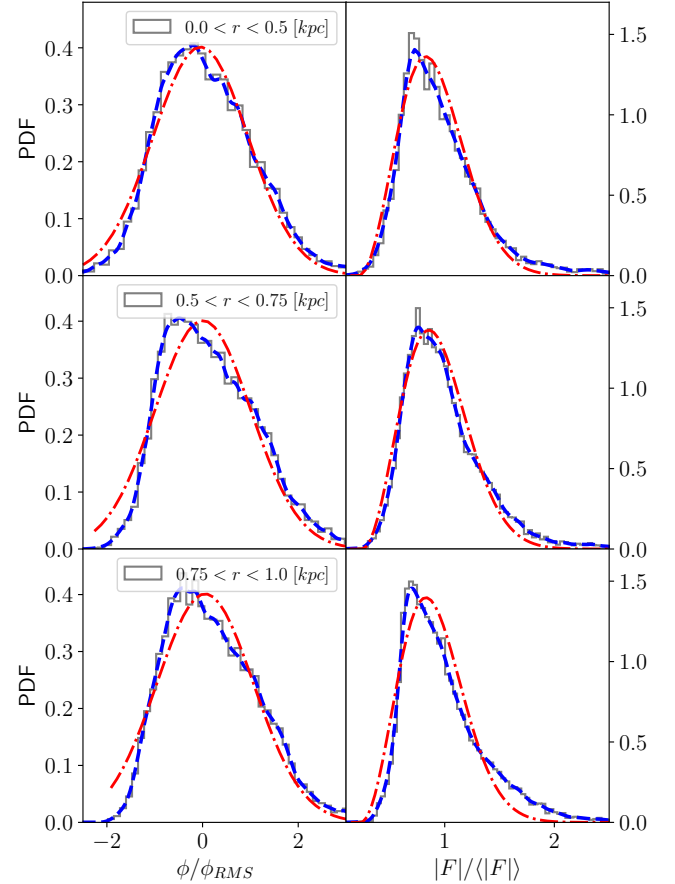


**Figure A2.** PDF of the fluctuations in the gas gravitational potential and the magnitude of the fluctuating force inside  $r = 1.0$  kpc. The fits (dashed-dotted red lines) are Gaussian for the potential fluctuations and Maxwellian (i.e., assumed to emanate from a Gaussian distribution in each degree of freedom, as suggested by Fig. A3) for the absolute value of the force.

fluctuations are well fit by Gaussians. Inside  $0.5r_s$  however they are better described by a lognormal distribution. This is not surprising, given that the mass fluctuations at these scales are quite large (as may also be probed from Fig. 6), and the density is bounded (by zero) from below but not necessarily from above. A similar situation, with analogous description, also appears in the description of large scale structure at large density contrasts (Coles & Jones 1991).

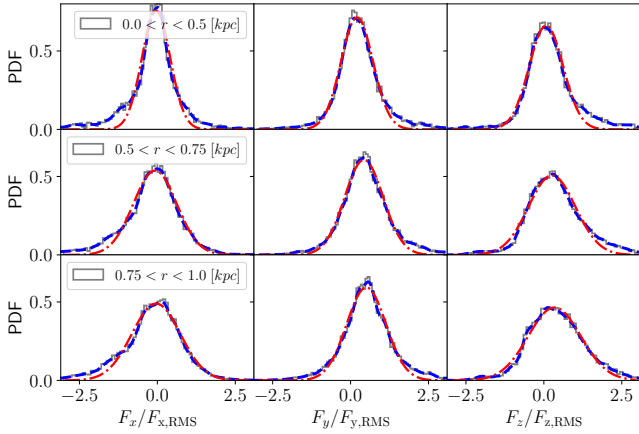


**Figure A3.** PDF of X,Y,Z components of force fluctuations with Gaussian fits (red dashed-dotted lines).

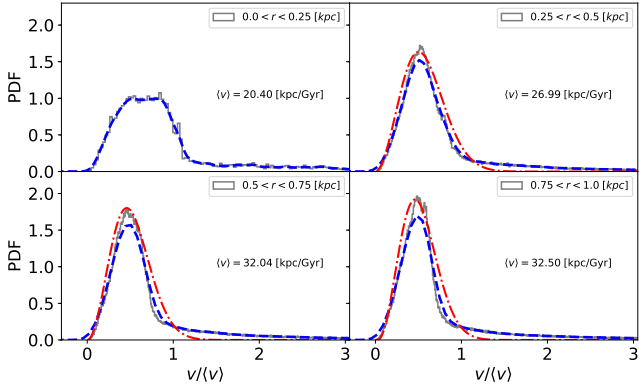


**Figure A4.** PDF of gas speeds, with Maxwellian fits at larger radial bins (red dashed-dotted lines).

The density and mass fluctuations do not however affect the dynamics directly. Rather what affects CDM trajectories are potential and force fluctuations. As the potentials and forces are related (through the Poisson equation) to the density through integrals, their fluctuations are generally milder in gravitational systems. We now examine these.

In order to obtain the gravitational field exerted by the gas perturbations on DM particles, we first sample random points inside a spherical region centred at the DM halo’s centre of potential. Then we calculate gas mass fluctuations defined as  $\delta M = M - \langle M \rangle$ , where  $\langle M \rangle$  is the average gas mass profile from the gas centre of mass. The gravitational potential of the gas perturbations is then obtained using:

$$\phi = \sum \frac{\delta M}{d}, \quad (\text{A1})$$

where  $d$  is the distance between a DM particle and gas points.

The gravitational force is directly obtained using the relations:

$$F_x = \sum \frac{\delta M}{d^2} \frac{x - x_c}{d}, \quad (\text{A2})$$

$$F_y = \sum \frac{\delta M}{d^2} \frac{y - y_c}{d}, \quad (\text{A3})$$

$$F_z = \sum \frac{\delta M}{d^2} \frac{z - z_c}{d}, \quad (\text{A4})$$

where  $x_c, y_c, z_c$  are the coordinates of the gravitational field centre.

The force amplitude is given as  $F = \sqrt{F_x^2 + F_y^2 + F_z^2}$ .

The results are shown in figures A2 and A3. Apart from modest departures — some long tail effects, as well as some skewness in the distribution of potential fluctuations — the fluctuating potential and force field is indeed Gaussian. This is particularly clear in the distribution of the force components shown in Fig. A3.

We note nevertheless that the modest but non-negligible non-Gaussianities imply that higher order moments of velocity perturbations ( $\langle (\Delta v)^m \rangle, m > 2$ ) may contribute to the effect of gas fluctuations; the departure of halo particle trajectories from their collisionless counterparts may involve corrections beyond the increase in velocity variance in the standard diffusion limit as described by (5). In standard two body relaxation, the long velocity tails arise from strong, close encounters, and are alleviated when the force perturbations are caused by extended structures (Peñarrubia 2019b). In our case, for power spectra  $\mathcal{P}(k) \sim k^{-n}$  with  $n > 0$ , the relaxation process is expected to be dominated by large scale modes (analogous to distant encounters the standard case); as equation (2) in fact emanates from an effective theory in which a higher scale  $k_x$  is eliminated when  $n > 0$  and  $k_x \gg k_m$  (cf. El-Zant et al. 2016 Section 2). The long tails here are thus likely to be due to halo particle interactions with rare large scale fluctuations (with large perturbing forces; cf. equation 33 of El-Zant et al. 2016). Their effect may be limited however by the flattening of the power spectrum at  $k < k_m$  (Fig. 4), and slow temporal variation of such modes (cf. Footnote 5). Verifying this, and comparing with theoretical formulations of anomalous diffusion (e.g. Bar-Or et al. 2013), may be of interest for further study of the dynamical effects of stochastic fluctuations with power law spectra considered here.

Finally we show in Fig. A4 the distribution of speeds of the gas fluid elements. This is calculated from the speeds in all gas cells within the indicated radii and the result is averaged over all time snapshots (excluding the first Gyr). At larger radial bins the speeds closely follow a Maxwellian distribution, (but with long tail at high speeds), with an average value saturating at  $\approx 30$  km/s. The speeds are smaller as one moves towards the centre.

## APPENDIX B: ENERGY INPUT AND CUTOFF IN THE HALO DISTRIBUTION FUNCTION

We obtain the phase space distribution  $f$  of halo particles by using the Eddington formula for a spherical density distribution with isotropic velocities (Binney & Tremaine 2008), by inserting numerical values for the dark matter potential and density inferred from the simulation. In Fig. B1 we plot the dimensionless distribution function of halo particles,  $F(\mathcal{E}) = f/(4\pi G)^{3/2} r_s^3 \rho_s^{1/2}$ , where  $\mathcal{E} = E/4\pi G \rho_s r_s^2$ , against  $1 + \mathcal{E}$ , which measures excess in energy above the minimum energy in the initial NFW system (i.e with zero point at  $\Phi_{\text{NFW}}(r = 0)$ ). Here one probes a cutoff in the distribution function at progressively larger values of  $1 + \mathcal{E}$ ; as the evolution progresses, halo particles migrate to higher energies as a result of their interaction with the fluctuating gas. Lower energy levels are emptied in the process.

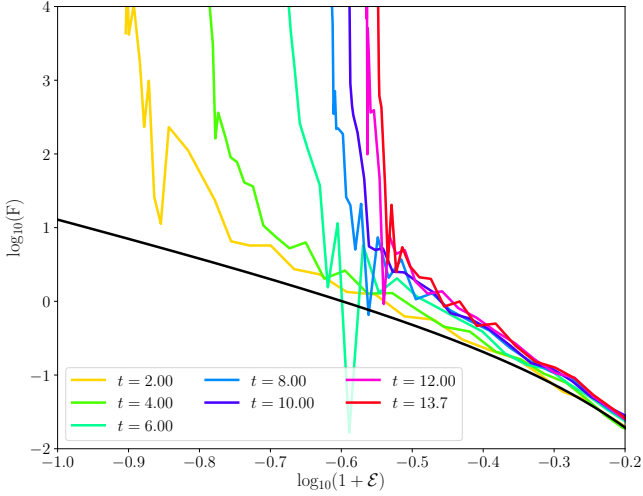


**Figure B1.** Dimensionless phase space distribution function  $F$  in terms of dimensionless energy  $\mathcal{E}$ , measured from the minimal energy in the initial NFW potential. In the initial NFW cusp the phase space density of halo particles continuously increases as the zero energy point of the NFW system (at  $\mathcal{E} = -1$ ) is approached. As energy is transferred from the fluctuating gas, however, a low energy cutoff in the distribution emerges, as particles migrate towards progressively higher energies.

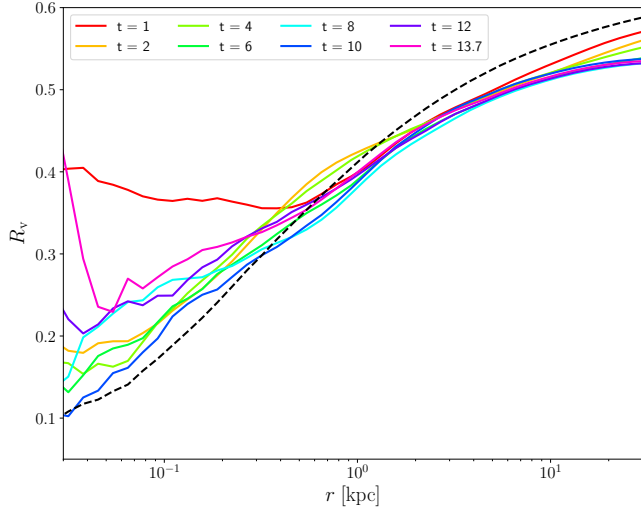


**Figure B2.** The ratio  $R = T_r/\Phi_r$ , where  $T_r = M \langle T_i \rangle$ ,  $\Phi_r = \frac{M}{2} \langle \Phi_i \rangle$ , and  $T_i$  and  $\Phi_i$  are halo particle specific kinetic energy and potential energies, and the averages are taken inside radii  $r$ .

We wish to relate this effect to the total energy input examined in Section 4, which is initially pumped into the particle trajectories in the form of kinetic energy. For this purpose, we may rewrite equation (8) in terms of the average kinetic and potential energies of the halo particles,

$$E_r = M \left( \langle T_i \rangle + \frac{1}{2} \langle \Phi_i \rangle \right), \quad (\text{B1})$$

where the averages are taken over all particles within radius  $r$  and  $M = M(< r)$  refers to the mass enclosed therein. Then we define

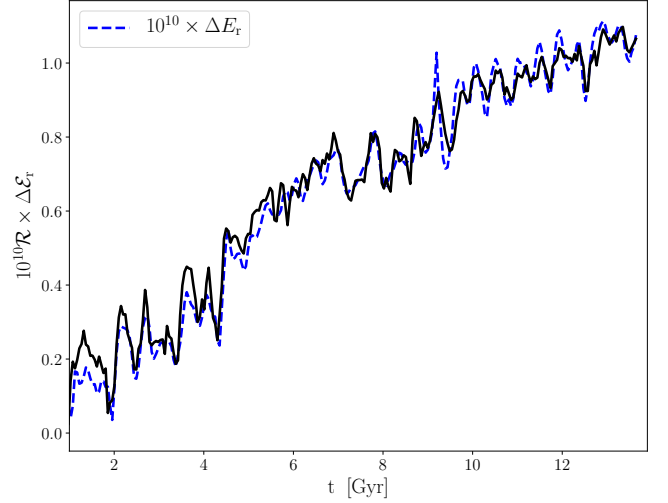


**Figure B3.** Comparison of total energy transferred from gas fluctuations to the halo (as in Fig. 7) with the average energy gained by dark matter particles evaluated *via* the cutoff in their distribution function  $\mathcal{E}_c$ . The latter is inferred from Fig. B1 and transformed through the factor  $\mathcal{R}$  from equation B5.

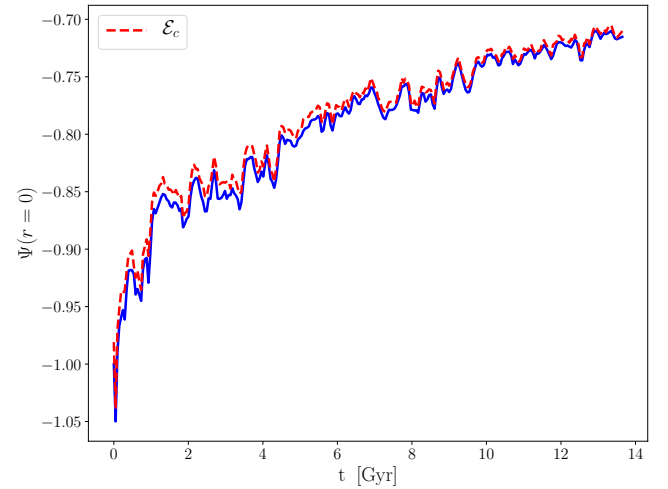


**Figure B4.** Comparison of the minimal dimensionless specific particle energy  $\mathcal{E}_c$  (corresponding to the energy cutoffs in Fig. B1) with that of the dimensionless potential  $\Psi = \Phi/4\pi G \rho_s r_s^2$  at  $r = 0$  (as in Fig. B1 the normalisation corresponds to the initial NFW parameters listed in Table 1).

$T_r = M \langle T_i \rangle$ ,  $\Phi_r = M \langle \Phi_i \rangle$  and  $R_v(r) = -T_r/\Phi_r$  such that

$$E_r = \frac{M}{2} (1 - R_v) \langle \Phi_i \rangle. \quad (\text{B2})$$

Also, using  $\langle E_i \rangle = \langle T_i \rangle + \langle \Phi_i \rangle$  and  $\langle T_i \rangle / \langle \Phi_i \rangle = -R_v/2$ ,

$$\langle E_i \rangle = \left( 1 - \frac{R_v}{2} \right) \langle \Phi_i \rangle. \quad (\text{B3})$$

And thus,

$$E_r = \frac{M}{2} \left( \frac{1 - R_v}{1 - \frac{R_v}{2}} \right) \langle E_i \rangle. \quad (\text{B4})$$

Fig. B2 shows the ‘virial ratio’  $R_v$  of the collection of halo particles within radius  $r$ . Within  $r_s$ , it is seen to vary from  $\sim 0.1$ , in the inner

region, to  $\sim 0.4$  at  $r \simeq r_s$ . The latter is the relevant value if we are interested in evaluating the average energy input within the initial NFW cusp.

To compare with the energy input inferred from Fig. 7, we first estimate the cutoff  $\mathcal{E}_c$  through the intersection of the distribution function with a horizontal line drawn around the maximum values in the distribution function in Fig. B1 (we don't explicitly draw this; it can be considered to correspond to the upper horizontal limiting line of the figure panel at  $F = 10^4$ ).

As with Fig. 7, we subtract the average over  $0.5 \leq t \leq 1.5$  Gyr from the numbers thus inferred and start our comparison at  $t = t_{\text{diff}} = 1$  Gyr (which is again our  $T = 0$  point). We denote the result by  $\Delta\mathcal{E}_r$ , and associate it with the average energy input per particle  $\langle \Delta E_i \rangle = (4\pi G \rho_s r_s^2) \Delta\mathcal{E}_r$ . The full transformation is then  $\Delta E_r = \mathcal{R} \Delta\mathcal{E}_r$ , with

$$\mathcal{R} = 2\pi G \rho_s r_s^2 M \left( \frac{1 - R_v}{1 - \frac{R_v}{2}} \right). \quad (\text{B5})$$

Fig. B3 shows the result of matching the total energy input at the saturation radial level (converging lines in Fig. 7), with  $\mathcal{R} \Delta\mathcal{E}_r$ , obtained as just described, assuming  $R_v = 0.4$  and  $M = M(< 1\text{ kpc})$  in equation (B5).

Finally we show that the dimensionless minimal cutoff energy scale  $\mathcal{E}_c$  in fact corresponds to the corresponding dimensionless potential ( $\Psi$ ) at  $r = 0$  (Fig. B4). This illustrates the process of energy redistribution; even if the initial energy is transferred from the gas to the halo particles in the form of kinetic energy, particles may still end up with zero kinetic energy, but still with increased energy as a result of a shallower self consistent potential well, corresponding to the formed core.

## APPENDIX C: FOKKER PLANCK FLUX FOR POWER LAW AND EXPONENTIAL DIFFERENTIAL ENERGY DISTRIBUTIONS

In this appendix we examine the three major simplifications made to arrive at equation (13). Namely, that the differential energy distribution may be approximated by its average value (equation 12); that the energy space flux of dark matter particles, migrating into higher energy levels under the influence of stochastic gas fluctuations, may be described in terms of the first order diffusion coefficient (as in equation 11); and that the flux through energy surface  $E$  due to the self consistent evolution of the system may likewise be absorbed in the parameter  $a$ .

In particular, we show how the assumption of absorbing the complexity of the situation in a single parameter  $a$  may be reasonable when the differential energy distribution may be approximated by a power law (which we will find to be the case in the region where the halo cusp is transformed into a core). We also show that this parameter is positive, allowing for outward mass flow, for systems with density decreasing with radius.

We finally discuss the qualitatively different behaviour at intermediate radii, where the differential energy distribution may be approximated instead by an exponential. In this latter case, the competing effects of the fluxes associated with the first and second order diffusion coefficients may cancel out, and the Fokker Planck flux may in fact vanish.

### C1 Approximating the differential energy distribution by its average

Consider a spherical density distribution  $\rho_p \propto r^\gamma$ , with  $-2 < \gamma < 0$ . If the distribution is infinite in radial extent, the potential  $\Phi(r)$ , defined in terms of the work done to take a particle to infinity, diverges. But  $\phi(r) \propto r^{-\beta}$ , associated with the work done in moving a particle from the centre to radius  $r$ , is well defined, and from the Poisson equation  $\gamma = -(\beta + 2)$ . One can also define the specific energy  $E_p = \phi(r) + \frac{1}{2}v^2$ . In the notation used in this work,  $E_p$  will correspond to  $E - E_0$  when  $\Phi(r)$  is well defined — as in the central region of a density distribution that, though well approximated by  $\rho_p \sim r^\gamma$  in the central region, eventually falls off sufficiently steeply with increasing radius. In this case  $\phi(r) = \Phi(r) - \Phi(0)$ .

For such power law systems, the mass weighed distribution function of a configuration with isotropic velocities can be written as  $g = g_0 E_p^{2/\beta - 1/2}$  and the density of states  $p = p_0 E_p^{1/2 - 3/\beta}$ , where  $g_0$  and  $p_0$  are positive constants (Evans 1994; El-Zant 2008). In general, the density of states corresponds to the area that encloses a phase space volume

$$q(< E) = \frac{16\pi^2}{3} \int_0^{r_{\text{max}}} [2(E - \Phi)]^{3/2} r^2 dE, \quad (\text{C1})$$

where  $r_{\text{max}}(E)$  is the maximum radius that a particle with specific energy  $E$  can reach. Thus  $p(E) = \partial q(< E) / \partial E$ .

The differential energy distribution is thus  $\partial M(< E_p) / \partial E_p = p g = p_0 g_0 E_p^{-1/\beta}$ , which for a power law distribution embedded in a larger halo tends to

$$\frac{\partial M(< E)}{\partial E} = p g = p_0 g_0 (E - E_0)^{-1/\beta}, \quad (\text{C2})$$

from where it also follows that

$$\frac{\partial M(< E)}{\partial E} = (1 - 1/\beta) \frac{M(< E)}{E - E_0}. \quad (\text{C3})$$

Therefore, for such systems, equation (12) becomes exact with  $a_p = 1 - 1/\beta = (3 + \gamma)/(2 + \gamma)$ , as mentioned in Section 4.3.

### C2 Use of first order diffusion coefficient

As the process of core formation proceeds on a significantly larger timescale than the dynamical time, one may use the orbit averaged Fokker Planck equation to describe the cumulative effect of small perturbations emanating from stochastic fluctuations (e.g. Spitzer 1987; Binney & Tremaine 2008). In flux conservation form, the mass change inside energy level  $E$  can then be written as (13) for an isotropic system (i.e., with  $g = g(E)$ ) may then be written as (El-Zant 2008)

$$\frac{\partial M(< E)}{\partial E} = -F_E + g \frac{\partial q}{\partial E}, \quad (\text{C4})$$

which says that a decrease in total mass of (in our case dark matter) particles with energy less than  $E$  is due to the Fokker Planck flux out of the volume enclosed by  $E$  in addition to changes in that volume resulting from the evolution in the structure of the system.

A major simplification leading to equation (13) involves the use of the first order energy diffusion coefficient  $D[\Delta E] = \langle \Delta E \rangle / T$ , the value of which is inferred directly from the simulation, instead of  $F_E$ . Theoretically however, terms associated with the second order coefficient  $D[(\Delta E)^2] = \langle (\Delta E)^2 \rangle / T$ , constitute a comparable contribution, as both coefficients involve the velocity variance  $\langle (\Delta v)^2 \rangle$ . Nevertheless, as we now show, if  $D[\Delta E]$  can be considered an energy independent constant, as assumed in equation (10), the total



flux is simply proportional to  $D[\Delta E]$ <sup>7</sup>. Furthermore, for power law systems, the inclusion of  $D[(\Delta E)^2]$  in the evaluation of the total flux leads to a simple rescaling that can be absorbed in a parameter  $a$ .

In general, for a spherical system with isotropic velocities, the orbit averaged Fokker Planck flux can be written as (e.g. El-Zant 2008)<sup>8</sup>

$$F_E = \left( D_E - D_{EE} \frac{\partial}{\partial E} \right) g, \quad (\text{C5})$$

where

$$D_E = pD[\Delta E] - \frac{1}{2} \frac{\partial}{\partial E} \left( pD[(\Delta E)^2] \right), \quad (\text{C6})$$

and

$$D_{EE} = \frac{1}{2} pD[(\Delta E)^2]. \quad (\text{C7})$$

As dark matter particles are too light to exchange energy through dynamical friction with the fluctuating gas field,  $\langle \Delta E \rangle = \frac{1}{2} \langle (\Delta v)^2 \rangle$ . Also, to leading order in perturbation  $\Delta \mathbf{v}/\mathbf{v}$ ,  $\langle (\Delta E)^2 \rangle = \langle (\mathbf{v} \cdot \Delta \mathbf{v})^2 \rangle = \frac{1}{3} v^2 \langle (\Delta v)^2 \rangle$  (e.g. Peñarrubia 2019a). If we assume that  $D[\Delta E]$  is independent of energy so will  $\langle (\Delta v)^2 \rangle$ . In this case, the first order energy diffusion coefficient is already orbit averaged, and averaging the second order one simply involves evaluating the mean of  $v^2$  over the energy shell of surface area  $p$ , which we denote by  $\langle v^2 \rangle_E$ . The Fokker Planck flux across that shell is then given by

$$F_E = D[\Delta E] \left[ pg - \frac{1}{3} \frac{\partial}{\partial E} \left( \langle v^2 \rangle_E pg \right) \right]. \quad (\text{C8})$$

The total flux is thus simply proportional to the first order coefficient  $D[\Delta E]$ .

Furthermore, for a power law region embedded in a larger halo, the density of states may be approximated by  $p = p_0(E - E_0)^{1/2-3/\beta}$ , and the corresponding  $\langle v^2 \rangle_E = 6\beta(3\beta - 6)^{-1}(E - E_0)$ , and thus

$$F_E = p_0 g_0 D[\Delta E] \left( \frac{6 + \beta}{6 - 3\beta} \right) (E - E_0)^{-1/\beta}, \quad (\text{C9})$$

From equations (C2), and (C3) this can be rewritten as

$$F_E = \left( \frac{(6 + \beta)(\beta - 1)}{\beta(6 - 3\beta)} \right) \frac{M(< E)}{E - E_0} D[\Delta E]. \quad (\text{C10})$$

Thus, for power law systems, the total flux is proportional to the flux associated with  $D[\Delta E]$  through a constant scaling factor (in brackets), that depends on the steepness of the power law. It is also always positive for systems with density decreasing with radius ( $\beta > -2$ ), allowing for mass outflow from stochastic fluctuations.

### C3 Self consistent evolution and evaluation of parameter $a$

To estimate the second term on the right hand side of equation (C4) we note that, from equation (C1),

$$\frac{\partial q}{\partial t} = -16\pi^2 \int_0^{r_{\max}} \frac{\partial \Phi}{\partial t} [2(E - \Phi)]^{1/2} r^2 dE. \quad (\text{C11})$$

<sup>7</sup> In the terminology of Sections 4.1 and 4.2, equation (10) effectively assumes a global energy input, with effective gas density  $\rho_0$  corresponding to the average density within the saturation radius  $r_{\text{sat}}$ , and parameters corresponding to those in equation 7

<sup>8</sup> Note that  $\langle \Delta E \rangle$  and  $\langle (\Delta E)^2 \rangle$  are defined there directly as the rates of changes of energy and its variance, and therefore are themselves the diffusion coefficients referred to here by  $D[\Delta E]$  and  $D[(\Delta E)^2]$ .

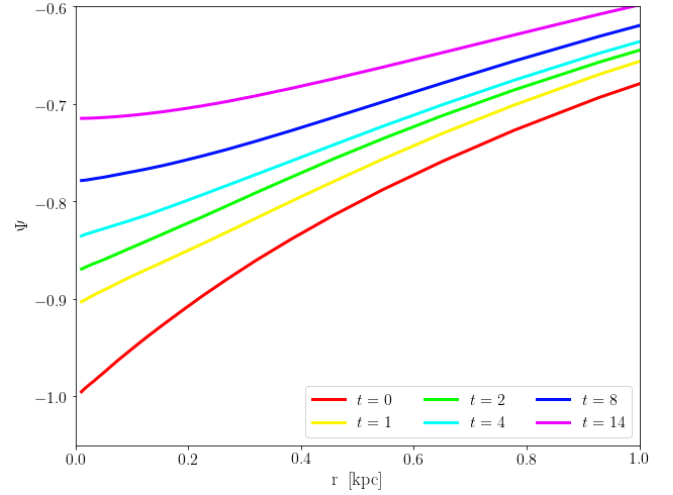


**Figure C1.** Dimensionless potential (defined as in Fig. B4) as a function of radius and time, as the central halo region evolves under the influence of the gas fluctuations.

Therefore the orbit averaged change of potential due to the self consistent evolution at energy  $E$  is then

$$\langle \dot{\Phi}(r) \rangle_E = -\frac{1}{p} \frac{\partial q}{\partial t}. \quad (\text{C12})$$

Recall that in Fig. B4 we found that the change of potential at the centre of the halo ( $r = 0$ ), resulting from the gas fluctuations, corresponds to the average energy gained per particle, taking into account the self consistent evolution of the system. Fig. B3, on the other hand, showed that that this corresponds to the average energy per unit mass pumped into the central halo multiplied by a factor  $\frac{2-R_v}{1-R_v}$ , with  $R_v = 0.4$ ; i.e., by a factor of about 2.7. Thus  $\dot{\Phi}_{E=E_0} = 2.7 \times D[\Delta E]$ . But, as can be seen Fig. C1, the change in the potential with time is significantly smaller at larger radii. Thus  $\dot{\Phi}_{E>E_0} < 2.7 \times D[\Delta E]$ ; at  $r = 1\text{kpc}$  (i.e., about the radius inside which the core forms) the total change is a bit more than a quarter of the value at  $r = 0$ . As the radial variation is not very steep we will approximate the change in energy due to evolution of the self consistent potential with an effective value, such that  $\dot{\Phi}_{\text{eff}} = \eta D[\Delta E]$ , where from the above considerations  $0.7 < \eta < 2.7$ . As we will see below, the mass particles within energy shell  $E$  increases steeply with energy away from the zero point in the central power law regions, with  $M(< E) \sim (E - E_0)^{2.3}$ . An effective value, replacing  $\langle \dot{\Phi}(r) \rangle_E$ , would thus correspond to more weight over larger energies, and therefore larger radii. We may thus expect  $\eta$  to be closer to its lower, rather than upper, limit.

Valid values of  $\eta$  are actually tightly constrained by the mass and density evolution in our model galaxy (Fig. 9), and the differential energy distribution in the inner halo. To see this we replace  $\partial q/\partial t$  by  $-p\eta D[\Delta E]$ , and use equation (C10), to rewrite equation (C4) as

$$\frac{\partial M(< E)}{\partial t} = - \left( \frac{(6 + \beta)(\beta - 1)}{\beta(6 - 3\beta)} + \eta \right) \frac{M(< E)}{E - E_0} D[\Delta E]. \quad (\text{C13})$$

This is equivalent to equation (13) if  $a$  is equal to the term in brackets. That is,

$$a = \frac{(6 + \beta)(\beta - 1)}{\beta(6 - 3\beta)} + \eta. \quad (\text{C14})$$

To determine  $\beta$  we need to show that the differential energy distribution of the inner halo may be fit by a power law and determine its

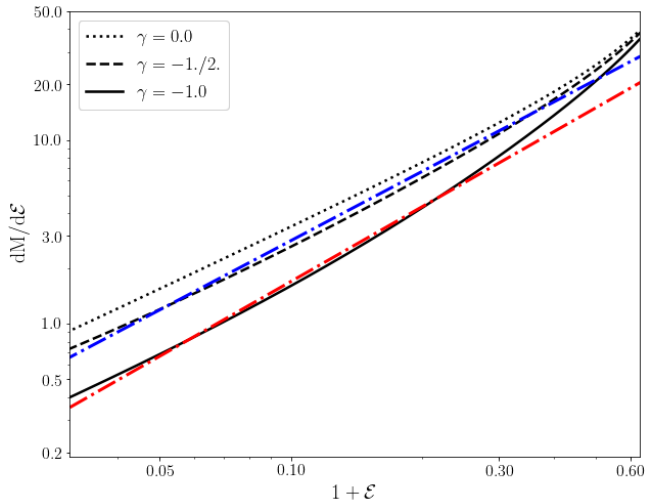


**Figure C2.** Differential energy distributions in the inner regions of three density profiles with  $\rho = \rho_s r^\gamma (1 + r/r_s)^{-3-\gamma}$ , where  $\gamma = -1$  for the NFW profile. The dimensionless energy  $\mathcal{E} = E/4\pi G\rho_s r_s^2$  is scaled such that the three profiles converge to the same densities as  $r \gg r_s$  (thus  $C = 1$  for the NFW,  $C = 3/2$  for  $\gamma = -1/2$  and  $C = 2$  for  $\gamma = 0$ ; cf. [Widrow 2000](#) for more details regarding these models). The dashed dotted lines are power law fits. The one fitting the NFW has slope 1.35. It approximates the differential energy distribution over energy scales  $0.03 \lesssim \mathcal{E} + 1 \lesssim 0.33$ , which enclose zero velocity spheres with radii of about 50pc and 1kpc in our simulation (with  $r_s = 0.88\text{kpc}$  as in Table 1), which correspond, respectively, to about the smallest radius inside which the halo density may be reliably resolved and the region inside which the gas fluctuations have significant effect on the halo profile. The dashed dotted line fitting the shallower profiles ( $\gamma = -1, 2, 0$ ) has only slightly flatter slope of 1.25.

index, in which case  $\beta$  is fixed by equation (C2). Fig. C2 shows that in the region where the core replaces the cusp the differential energy distribution of an NFW profile may indeed be fit by a power law, with index of about 1.35, which corresponds to  $\beta = -0.74$ . Furthermore, as can also be seen from Fig. C2 the differential energy slopes of models with the same asymptotic physical density distribution for  $r \gg r_s$ , but have milder inner cusps ( $\gamma = -1/2$ ), or even cores ( $\gamma = 0$ ), can be approximated by similar power laws (with  $\beta \approx -0.8$ ), suggesting that the power law approximation may hold as the cusp transforms into core.

Furthermore, in Section 4.3 we found that a value of  $2.5 \lesssim a \lesssim 2.8$  can be used to obtain solutions to equation (13) that describe the mass and density evolution fairly well (Fig. 9, right hand panel). For the aforementioned values of  $\beta$ , this corresponds to  $1 \lesssim \eta \lesssim 1.4$ , which is within the expected range inferred above.

#### C4 The vanishing of the flux for exponential differential energies (and constant dispersion)

At larger energies, corresponding to intermediate radii beyond  $r_s$ , the differential energy distribution is better approximated by an exponential, rather than a power law, as Fig. C3 illustrates. At such radii, the halo is nearly isothermal, with density  $\rho_p \sim 1/r^2$ , and  $\langle v^2 \rangle_E$  approximately constant. Assuming this, and inserting  $\partial M(< E)/\partial E \propto e^{\beta E}$  into (C8), it is easily seen that the flux is nullified if  $\beta = 1/\sigma^2$ , where  $\sigma^2 = \frac{1}{3}\langle v^2 \rangle$  is the one dimensional velocity variance. This may explain the formation of cores up to the region where the differential energy distribution may be approximated by a power law, where the

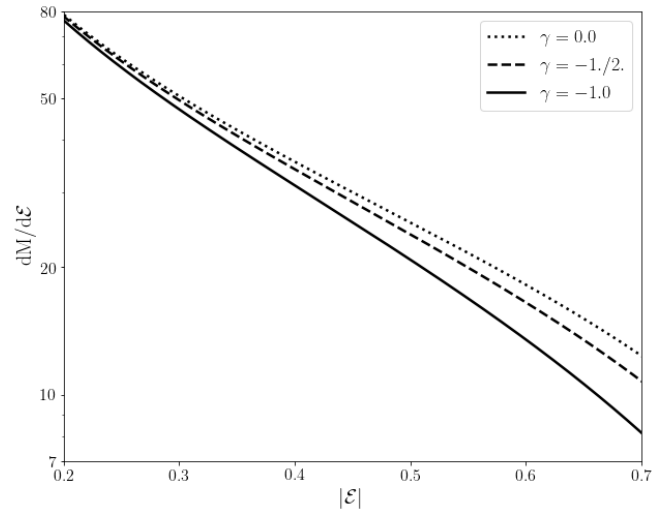


**Figure C3.** The differential energy distributions of the models of Fig. C2 in the intermediate energy range, where the quasi-linear variation on the log-linear plot suggests an exponential scaling, particularly for  $0.35 \lesssim |\mathcal{E}| \lesssim 0.65$ , corresponding to zero velocity spheres with radii of about 1.4 and 4.7 kpc in our model galaxy.

flux is positive, but that the response to fluctuations is more robust when the exponential is a better approximation.

This paper has been typeset from a  $\text{\TeX}/\text{\LaTeX}$  file prepared by the author.